COUPLED EFFECTIVE STRESS ANALYSIS OF INSERTION PROBLEMS IN GEOTECHNICS WITH THE PARTICLE FINITE ELEMENT METHOD

Lluís Monforte[a], Marcos Arroyo[a], Josep Maria Carbonell[b] & Antonio Gens[a].

a Universitat Politècnica de Catalunya – BarcelonaTech

Department of Geotechnical Engineering,

Campus Nord UPC, Gran Capità s/n

08034 Barcelona

lluis.monforte@upc.edu; marcos.arroyo@upc.edu; antonio.gens@upc.edu

b International Center for Numerical Methods in Engineering (CIMNE),

Campus Nord UPC, Gran Capità s/n

08034 Barcelona

cpuigbo@cimne.upc.edu

ABSTRACT:

This paper describes a computational framework for the numerical analysis of quasi-static soil-structure insertion problems in water saturated media. The Particle Finite Element Method is used to solve the linear momentum and mass balance equations at large strains. Solid-fluid interaction is described by a simplified Biot formulation using pore pressure and skeleton displacements as basic field variables. The robustness and accuracy of the proposal is numerically demonstrated presenting results from two benchmark examples. The first one addresses the consolidation of a circular footing on a poroelastic soil. The second one is a parametric analysis of the cone penetration test (CPTu) in a material described by a Cam-clay hyperelastic model, in which the influence of permeability and contact roughness on test results is assessed.

KEYWORDS

Penetration test, Large strains, Particle Finite Element Method (PFEM), Cone penetration test.

COUPLED EFFECTIVE STRESS ANALYSIS OF INSERTION PROBLEMS IN GEOTECHNICS WITH THE PARTICLE FINITE ELEMENT METHOD

This paper describes a computational framework for the numerical analysis of quasi-static soil-structure insertion problems in water saturated media. The Particle Finite Element Method is used to solve the linear momentum and mass balance equations at large strains. Solid-fluid interaction is described by a simplified Biot formulation using pore pressure and skeleton displacements as basic field variables. The robustness and accuracy of the proposal is numerically demonstrated presenting results from two benchmark examples. The first one addresses the consolidation of a circular footing on a poroelastic soil. The second one is a parametric analysis of the cone penetration test (CPTu) in a material described by a Cam-clay hyperelastic model, in which the influence of permeability and contact roughness on test results is assessed.

1. Introduction

Many activities in geotechnical engineering (probing, sampling, pile installation….) involve the insertion of a rigid body into the soil. In this kind of problem, large displacements and deformations of the soil mass always occur. The coupled hydro-mechanical response of the soil adds further complexity, even in cases where insertion speed is tightly controlled. Analysis of problems of rigid body insertion into soil masses had traditionally relied on highly idealized approaches such as geometrically simple cavity expansion mechanisms (Yu & Mitchell, 1998). Although much insight is gained from such analyses, a number of basic features of the problem are left aside and, as a consequence, a host of not fully understood empirical corrections and methods have been relied upon for practical applications. Current interpretation of CPTu results (Mayne, 2007; Schnaid, 2009; Robertson & Cabal, 2015) is a clear example.

Numerical simulation seems an obvious alternative to advance understanding in this area. However, the numerical simulation of rigid body insertion into soils is a complex task because the system exhibits many non-linearities, contact-related, material-related and also geometrical. The geometrical non-linearity was a fundamental obstacle to the Lagrangian formulations of the finite element method (FEM) that are successful in other areas of geotechnical engineering. Strong mesh distortion resulted in large inaccuracies and/or stopped calculation at relatively small displacements (De Borst & Vermeer, 1984).

In the last decades several numerical frameworks have been developed to address those problems. Some approaches are not based on continuum mechanics and use instead discrete element methods (Arroyo et al. 2011; Ciantia et al. 2016). Continuum-based approaches are however dominant, particularly for fine-grained soils. Within continuum-based methods the approach most frequently applied to geotechnical insertion problems has been that of Arbitrary Lagrangian-Eulerian formulations (ALE). ALE finite element formulations combine the Lagrangian and Eulerian kinematic descriptions, by separately considering material and computational mesh motions (Donea et al. 2004). Several slightly different ALE methods have been applied in geomechanics; a comparative review was recently presented by Wang et al. (2015).

A second continuum-based numerical framework is that of the Material Point Method (MPM). A set of particles (material points) move within a fixed finite element computational grid. Material points carry all the information (density, velocity, stress, strain, external loads…) which, at each step, is transferred to the grid to solve the mechanical problem. The computed solution allows updating of position and properties of the material points. Several implementations of MPM have been already used to model rigid body insertion into soils (Sołowski & Sloan, 2015; Ceccato et al. 2016 a,b).

The Particle Finite Element Method (PFEM) is a third continuum-based approach that seems suitable to address geotechnical insertion problems. PFEM is actually an updated Lagrangian approach, but one that avoids mesh distortion problems by frequent remeshing. The nodes discretizing the analysis domain are treated as material particles the motion of which is tracked during the numerical solution. Remeshing in PFEM is based in Delaunay tessellations and uses low-order elements. PFEM was first developed to solve fluid-structure interaction problems (Oñate et al. 2004) and then extended to other areas, like erosion, solid-solid interaction and thermo-plastic problems (Oñate et al. 2011, Rodriguez et al, 2016).

Within geomechanics, PFEM was initially applied to tool-rock interaction problems by Carbonell et al (2010, 2013). Later, Salazar et al (2016), extended that code to include Bingham-like rheology to model flowslides. Zhang et al (2013, 2017) have also used PFEM in the context of soil flow problems.

G-PFEM is a PFEM-based code for the analysis of solid insertion problems in soils. G-PFEM has been implemented into Kratos (Dadvand et al. 2010), an object-oriented multi-disciplinary open-access platform for numerical analysis tool development. Previously (Monforte et al. 2017a), the authors have demonstrated the good performance of G-PFEM in total stress analysis. In Monforte et al. (2017b), the numerical stabilization techniques that underpin the method, both for the single phase and for two-phase cases, was presented in detail.

This work documents G-PFEM developments to model two-dimensional coupled hydromechanical problems for water-saturated soils in quasi-static conditions. Some initial developments along this line were briefly illustrated by Monforte et al (2015) and Gens et al (2016). The paper is structured in two main sections. The first one presents the main features of the numerical method: governing equations, discretization, stabilization and mixed formulations, constitutive relations and the contact model. The second one illustrates the performance of the method in two reference problems: consolidation of a circular footing loading a poroelastic soil and CPTu insertion into a modified cam clay soil of varying permeability.

2. Numerical model

2.1 PFEM

PFEM is a mesh-based continuum method: the solution is computed in a finite element mesh built with well-shaped low order elements. This computational mesh evolves during problem solution by means of frequent remeshing. A cornerstone of the PFEM implementation used here is an efficient remeshing strategy (Oñate et al. 2004). Basic tasks used in that strategy include adaptive inclusion of new nodes, Delaunay tessellation based on nodes and element

smoothing. A Lagrangian description of the continuum is used and information between meshes is transferred using interpolation algorithms. This general PFEM scheme is enriched with the inclusion of rigid bodies of specified motion that may contact, penetrate and reshape the discretized continuum.

Although it is not strictly necessary (e.g. Zhang et al. 2013), low order finite elements are typically used in PFEM: linear triangles in two-dimensional models and linear tetrahedra in three dimensions. Linear interpolated elements have several advantages based on their simplicity: particles usually define exclusively the mesh nodes and no additional interpolations are needed after remeshing. The computational cost is also reduced with respect to high-order elements, even if stabilized mixed formulations are required.

The interpolation of state variables plays a crucial role in the accuracy of the results. To avoid excessive smoothing of internal variables, information is transferred from the previous Gauss points to the new ones. In this work, a nearest neighbor interpolation procedure is used; hence, new integration points inherit the information of the closer Gauss point of the previous mesh. This strategy ensures that information is maintained in elements that do not change during the meshing process. When new particles are inserted in the domain, variables are linearly interpolated from those of the previous mesh element. More details about remeshing and interpolation in PFEM can be found elsewhere (Monforte et al. 2017a; Rodriguez et al. 2016).

PFEM has some commonalities with some ALE methods previously used in geomechanics, like the remeshing and interpolation technique by small strain (RITSS) (Hu & Randolph, 1998) or the so-called efficient ALE approach (EALE) (Nazem et al. 2006); a discussion of similarities and differences with those techniques may be found in Monforte et al. (2017a).

2.2 Governing equations

We consider only water saturated soils. They are modeled as a two-phase continuum employing a finite deformation formulation. The equations of linear momentum and mass of the mixture are written following the movement of the solid skeleton, considering as unknown fields the solid skeleton displacements and fluid pressure. This is the $\boldsymbol{u}$-p_w formulation, an approximation of the generalized Biot equations valid at moderate velocities (Zienkiewicz et al. 1980). For pseudo-stationary cases, these equations may be expressed as (Borja & Alarcón, 1995; Larsson & Larsson, 2012):

$$\begin{cases} \nabla \cdot \boldsymbol{\sigma} + \rho_m \boldsymbol{g} = \boldsymbol{0} & \text{in } \Omega_t \times (0,T) \\ \dfrac{\varphi}{K_w}\dot{p}_w + \nabla \cdot \boldsymbol{v} + \nabla \cdot \boldsymbol{v^d} = 0 & \text{in } \Omega_t \times (0,T) \\ \boldsymbol{u}(\boldsymbol{X}, t=0) = \boldsymbol{u_0} & \text{in } \Omega_0 \\ p_w(\boldsymbol{X}, t=0) = p_{w0} & \text{in } \Omega_0 \\ \boldsymbol{u}(\boldsymbol{X}, t) = \bar{\boldsymbol{u}} & \text{in } \Gamma_{\bar{\boldsymbol{u}}} \times (0,T) \\ \boldsymbol{n} \cdot \boldsymbol{\sigma} = \boldsymbol{t} & \text{in } \Gamma_{\bar{\boldsymbol{t}}} \times (0,T) \\ p_w(\boldsymbol{X}, t) = \bar{p}_w & \text{in } \Gamma_{\bar{p}} \times (0,T) \\ -\boldsymbol{n} \cdot \boldsymbol{v^d} = j & \text{in } \Gamma_{\bar{j}} \times (0,T) \end{cases} \tag{1}$$

where $\boldsymbol{\sigma} = \boldsymbol{\sigma}' - p_w \boldsymbol{1}$ is the total Cauchy stress tensor, $\boldsymbol{\sigma}' = \widehat{\boldsymbol{\sigma}'}(\boldsymbol{F}, V)$ is the effective Cauchy stress tensor, $\widehat{\boldsymbol{\sigma}'}$ stands for the appropriate constitutive equation for path dependent

materials, $\boldsymbol{F}$ is the total deformation gradient whereas V represents the set of internal variables of the constitutive model. ρ_m is the spatial description of the soil density, defined as $\rho_m = (1-\varphi)\rho_s + \varphi\,\rho_w = \frac{\rho_m^0}{J} + \frac{J-1}{J}\rho_w$, ρ_s and ρ_w are the density of the solid and water phase respectively. φ is the porosity, whose variations changes in time due to deformation and it is actualized according to : $\varphi = 1 - \frac{1-\varphi_0}{J}$, where φ_0 is the initial state whereas $J = \det(\boldsymbol{F})$ is the Jacobian between the initial state and the deformed configuration. It is assumed that the solid phase is incompressible, whereas the water phase is almost incompressible, with bulk volume stiffness given by K_w.

A Large strain generalization of Darcy's law (Carter et al, 1979; Larsson and Larsson, 2002) is employed:

$$\boldsymbol{v}^d = -\boldsymbol{k}\,(\nabla p_w - \rho_w \boldsymbol{g}) \tag{2}$$

where $\boldsymbol{k}$ is the permeability tensor. When permeability is anisotropic it is advantageous to consider it constant in the material description and rotate it following the solid skeleton deformation (Larsson and Larsson, 2002). Anisotropic and void-ratio dependent (Kozeny-Carman (Chapuis & Aubertin (2003)) permeability definitions have been implemented in GPFEM (Hauser, 2017) but they are not considered further in here; all cases presented use a constant isotropic value of permeability, denoted *k*.

2. 3 Weak form and discretization

The weak form of equation (1) is obtained following standard procedures (Zienkiewicz & Taylor, 2005), multiplying both field equations by a set of virtual displacements, $\boldsymbol{w}$, and virtual water pressure, q, integrating the equations over the deformed domain, Ω_t, and applying the divergence theorem:

$$\begin{cases} \int_{\Omega_t} \frac{\partial w_i}{\partial x_j}(\sigma'_{ji} - p_w\delta_{ij})\mathrm{d}\Omega_t = \int_{\Omega_t} w_i\,\rho_m b_i\,\mathrm{d}\Omega_t + \int_{\Gamma_{\bar{t}}} w_i\,t_i\,\mathrm{d}\gamma \\ \int_{\Omega_t} q\left(\frac{\dot{p}_w}{K_w} + \frac{\partial v_i}{\partial x_i}\right)\frac{1}{J}\,\mathrm{d}\Omega_t + \int_{\Omega_t}\frac{\partial q}{\partial x_i}v_i^d\frac{1}{J}\mathrm{d}\Omega_t = \int_{\Gamma_{\bar{j}}} qj\frac{1}{J}\,\mathrm{d}\gamma \end{cases} \tag{3}$$

Note that the integration of the mass balance equation takes place over the reference domain. This is not the only possibility and, for instance, Borja and Alarcón (1995) integrate the mass balance equation directly over the current configuration (in other words, multiplying the equation by J) whereas Larsson and Larsson (2002) formulate the mass balance in terms of fluid content (i.e, scaling the equation by $J\,\rho_w$).

After obtaining the weak form of the balance equations, the discrete equations of the hydromechanical formulation are obtained. First, let us introduce the interpolants:

$$\begin{cases} \boldsymbol{u} \approx \boldsymbol{u}^h = \boldsymbol{N}_u \cdot \tilde{\boldsymbol{u}} \\ \boldsymbol{w} \approx \boldsymbol{w}^h = \boldsymbol{N}_u \cdot \tilde{\boldsymbol{w}} \\ p_w \approx p_w^h = \boldsymbol{N}\cdot\widetilde{\boldsymbol{p_w}} \\ q \approx q^h = \boldsymbol{N} \cdot \tilde{q} \end{cases} \tag{4}$$

where $\boldsymbol{u}^h$ is the finite element approximation of the field $\boldsymbol{u}$ whereas $\tilde{\boldsymbol{u}}$ are the nodal values. $\boldsymbol{N} = [N_1, N_2, \dots, N_n,]$ and $\boldsymbol{N}_u = [N_1\mathbf{1}, N_2\mathbf{1}, \dots, N_n\mathbf{1}]$ are the shape functions, identical for the displacement and water pressure fields.

Introducing the spatial discretization and using a fully implicit time marching scheme, the governing equations read:

$$\begin{cases} \boldsymbol{P}\left({}^{n+1}\boldsymbol{\sigma}'\right) - \boldsymbol{Q} \cdot \widetilde{{}^{n+1}\boldsymbol{p}_w} = \boldsymbol{f}^{ext} \\ \boldsymbol{Q}^{*T} \cdot \Delta\,\tilde{\boldsymbol{u}} + \dfrac{1}{K_w}\boldsymbol{M}\,\Delta\widetilde{\boldsymbol{p}_w} - \Delta t\,\boldsymbol{H}\,\widetilde{{}^{n+1}\boldsymbol{p}_w} = \Delta t\,\boldsymbol{f}^{pw} \end{cases} \tag{5}$$

where the velocity is approximated as $\boldsymbol{v} \approx \frac{\Delta \boldsymbol{u}}{\Delta t} = \frac{{}^{n+1}\boldsymbol{u} - {}^{n}\boldsymbol{u}}{\Delta t}$ and the material time derivative of the water pressure with respect to the solid skeleton as $\dot{p}_w = \frac{\Delta p_w}{\Delta t} \approx \frac{{}^{n+1}p_w - {}^{n}p_w}{\Delta t}$. Note that the definition of the Darcy's law has been introduced in matrix $\boldsymbol{H}$. Detailed expressions for all matrices appearing in the governing equations are given in the Appendix.

2.4 Stabilization

The governing discretized equations in GPFEM are jointly inverted in a monolithic solution. Therefore, using equal order interpolants for displacement and water pressure fails to satisfy the *inf-sup* stability condition in the undrained limit (Pastor et al, 1999). As a result, large amplitude spatial oscillations appear on the water pressure field, and stiffer responses are observed in the system. To avoid this problem several numerical techniques are available. The most popular uses displacement interpolants one order higher than those in the water pressure field. Another technique, which is the one adopted here, is the inclusion of stabilizing terms in the field equations.

To stabilize the mass conservation equation, the Polynomial Pressure Projection technique (PPP) is used (Bochev et al, 2006; Sun et al, 2013). That means that the following term is added to the weak form of the mass balance equation of the hydromechanical problem:

$$\sum_e \int_{\Omega_e} (q - \check{q})\,\tau(p_w - \check{p}_w)\,\mathrm{d}\Omega_\mathrm{t} \tag{6}$$

where τ stands for the stabilization parameter and $\check{q}$ and $\check{p}_w$ are the best approximations of the virtual water pressure and water pressure in the space of polynomials of one order less than the shape functions (which, in our case, are simply constant-valued functions) .

The stabilization term has similar effect on the output as the minimal time step stability conditions that are applied for implicit FE time integration of consolidation problems (Cui et al. 2016). Indeed, a similar analytical procedure as that employed by Cui et al. (2016) to obtain an stable time step limit was used here to establish an evaluation rule for the stabilization parameter, τ. The stabilization parameter in each element is obtained as:

$$\tau = \begin{cases} \dfrac{2}{M} - \dfrac{12\,k\,\Delta t}{g\,\rho_w\,h_e^2} & \Delta t < \dfrac{h_e^2}{6\,c_v} \\ 0 & \Delta t \geq \dfrac{h_e^2}{6\,c_v} \end{cases} \tag{7}$$

where M is the constrained modulus, h_e is the element size and $\boldsymbol{c_v} = M\,k/(g\,\rho_w)$ is the consolidation coefficient.

2.4 Mixed formulation

Incompressibility in soils may not only arise from the hydro-mechanical response (i.e, undrained conditions) but also from the effective response of the medium. This is the case, for example, when failure is reached in Critical State soil models, as a constant volume condition defines the behavior at the Critical State Line.

To deal with this second source of incompressibility mixed formulations have been proven effective (Sun et al, 2013). In a previous work (Monforte et al. 2017b), the authors explored in detail several alternatives of mixed formulations for the hydromechanical problem. The formulation that showed best performance was the displacement-Jacobian (or Volume change) -Water-pressure ($\boldsymbol{u} - \theta - p_w$) formulation and it is employed here. In essence the effective response of the medium is computed with an assumed deformation gradient, $\bar{\boldsymbol{F}}$, whose deviatoric part is computed as usual whereas its volumetric part is approximated by the Jacobian, θ. A separate field equation is introduced to express that approximation, an equation that is also stabilized using the PPP technique. Further details are given in Monforte et al (2017b).

2.5 Constitutive relations

The constitutive equations are formulated in a large strain framework. For the first example below, a purely linear elastic response is assumed between the Kirchhoff stress and the Hencky (or logarithmic) strain:

$$\boldsymbol{\tau}' = K\varepsilon_v^e\mathbf{1} + 2G\boldsymbol{\varepsilon}_d^e \tag{8}$$

For more realistic modelling of soil behavior, large strains elasto-plastic constitutive equations are generally employed. These models are based on a multiplicative split of the deformation gradient into elastic and plastic parts and the use of a hyperelastic model (Simo & Hughes, 1998). At the price of some added complexity, hyperelastic constitutive equations have the advantage of ensuring thermodynamic consistency (Houlsby et al, 2005).

Here the hyperelastic model first proposed by Houlsby (1985) and later modified by Borja et al (1997) is used. The main feature of the model is that it is able to capture the pressure-dependent nature of the bulk and shear modulus by defining them as a function of the first and second invariants of the deformation measure (Housbly, 1985; Borja et al, 1997).

Using the computational geomechanics sign convention (that is, compression is considered as negative), the stored energy function, $\psi(\boldsymbol{\varepsilon^e})$, is then given by:

$$\psi(\boldsymbol{\varepsilon^e}) = p_0\kappa^* \exp\left(\frac{-\varepsilon_v^e}{\kappa^*}\right)\left(1 + \frac{\alpha}{\kappa^*}\|\boldsymbol{\varepsilon_d^e}\|^2\right) + G_0\|\boldsymbol{\varepsilon_d^e}\|^2 \tag{9}$$

where $\boldsymbol{\varepsilon^e} = \frac{\ln(\boldsymbol{b^e})}{\mathbf{2}}$ is the elastic Hencky strain tensor, $p_0 > 0$ a reference pressure whereas $G_0 \geq 0$ and $\alpha \geq 0$ are two parameters of the model, $\kappa^* = \frac{\kappa}{1+e_0}$ and κ is the swelling slope. The effective Kirchhoff stress, $\boldsymbol{\tau}'$, is computed according to:

$$\boldsymbol{\tau}' = \frac{\boldsymbol{\sigma}'}{J} = \frac{\partial \psi(\boldsymbol{\varepsilon^e})}{\partial \boldsymbol{\varepsilon^e}} = -p_0 \exp\left(\frac{-\varepsilon_v^e}{\kappa^*}\right)\left(1 + \frac{\alpha}{\kappa^*}\|\boldsymbol{\varepsilon_d^e}\|^2\right)\mathbf{1} + 2\left(G_0 + \alpha p_0 \exp\left(\frac{-\varepsilon_v^e}{\kappa^*}\right)\right)\boldsymbol{\varepsilon_d^e} \quad (10)$$

where the first term stands for the effective pressure whereas the second one represents the deviatoric stresses and $\mathbf{1}$ is the second order identity tensor. Then, the following tangent matrix may be obtained:

$$\boldsymbol{D} = \frac{\partial^2 \psi(\boldsymbol{\varepsilon^e})}{\partial \boldsymbol{\varepsilon^{e\,2}}} = \frac{\partial \boldsymbol{\tau}'}{\partial \boldsymbol{\varepsilon^e}} = K\,\mathbf{1} \otimes \mathbf{1} + G\,\boldsymbol{I^D} + C(\mathbf{1} \otimes \frac{\boldsymbol{\varepsilon_d^e}}{\|\boldsymbol{\varepsilon_d^e}\|} + \frac{\boldsymbol{\varepsilon_d^e}}{\|\boldsymbol{\varepsilon_d^e}\|} \otimes \mathbf{1}) \quad (11)$$

where:

$$K = \frac{p_0}{\kappa^*}\exp\left(\frac{-\varepsilon_v^e}{\kappa^*}\right)\left(1 + \frac{\alpha}{\kappa^*}\|\boldsymbol{\varepsilon_d^e}\|^2\right) = \frac{-\pi'}{\kappa^*} \quad (12)$$

$$G = G_0 + \alpha p_0 \exp\left(\frac{-\varepsilon_v^e}{\kappa^*}\right) \quad (13)$$

$$C = -2\frac{\alpha}{\kappa^*} p_0 \exp\left(\frac{-\varepsilon_v^e}{\kappa^*}\right)\|\boldsymbol{\varepsilon_d^e}\| \quad (14)$$

where $\pi' = p'/J$ is the Kirchhoff effective pressure. These last equations show that if $\alpha > 0$ then $C \neq 0$ and the volumetric and deviatoric elastic behavior is coupled.

The modified Cam-clay model is completed specifying the yield surface and the hardening law:

$$f(\boldsymbol{\tau}') = \left(\frac{\sqrt{3}J_2}{M(\theta_L)}\right)^2 + \pi'(\pi' - p_c) \quad (15)$$

$$p_c = -p_{c0}\exp\left(\frac{-\varepsilon_v^p}{\lambda^* - \kappa^*}\right) \quad (16)$$

where $p_{c0} > 0$ is the reference preconsolidation pressure, $\lambda^* = \frac{\lambda}{1+e_0}$, λ is the slope of the virgin consolidation line and M is the slope of the critical state line in the $\pi' - \sqrt{3J_2}$ plane. The shape adopted for the yield surface in the deviatoric plane is a convex reformulation of the Matsuoka-Nakai failure criterion (Panteghini & Lagioia, 2014) that may simply be described as a smoothed generalization of the Mohr-Coulomb criterion.

Associated plasticity is assumed. The integration of the elasto-plastic constitute relations is performed with an explicit scheme, which is an extension of Sloan's scheme at large strains (Sloan et al. 2001). The scheme considers adaptive substepping and correction for the yield surface drift and it is described elsewhere (Monforte et al, 2014, 2017a)

2.6 Contact model

The problems analyzed typically involve contact between a very rigid object and deformable soil. A simple way to model such contact describes the rigid object by a parametrized surface that imposes contact constraints on the soil using the Penalty Method (Wriggers, 2006). With

this approach, an additional term due to the contact contribution is added to the linear momentum balance equation:

$$C_c = \int_{\gamma_c} \boldsymbol{w} \cdot (\sigma_n \boldsymbol{n} + \boldsymbol{t})\, \mathrm{d}\gamma \tag{17}$$

where γ_c is the part of the boundary in contact, σ_n is the normal total contact stress, $\boldsymbol{n}$ is the outwards normal whereas $\boldsymbol{t}$ stands for the tangential contact stress.

The total normal stress acting on the contact is obtained as:

$$\sigma_n = \epsilon\, g_n^- \tag{18}$$

where ϵ is the penalty parameter and g_n^- is the penetration function. That is, the normal stress is proportional to the amount of the penetration of the deformable body into the rigid structure.

The tangential part of the contact condition is modelled using an elasto-plastic analogy (Wriggers, 1995; Wriggers, 2006) in terms of effective stress. In this approach the so-called stick conditions corresponds to the elastic regime, whereas the slip conditions are represented by the plastic flow. The model may be expressed as:

$$\begin{cases} \boldsymbol{g}_t = \boldsymbol{g}_t^e + \boldsymbol{g}_t^s \\ \mathrm{L}_v\, \boldsymbol{t} = \epsilon_t \dot{\boldsymbol{g}}_t^e \\ f_s(\boldsymbol{t}, \sigma'_n, g_v) = |\boldsymbol{t}| - \overline{f_s}(\sigma'_n, g_v) \le 0 \\ \dot{\boldsymbol{g}}_t^s = \dot{\gamma}\, \dfrac{\partial f_s}{\partial \boldsymbol{t}} = \dot{\gamma}\, \dfrac{\boldsymbol{t}}{|\boldsymbol{t}|} \\ \dot{g}_v = \dot{\gamma} \end{cases} \tag{19}$$

where $\boldsymbol{g}_t$ is the tangential gap that decomposes in an elastic, $\boldsymbol{g}_t^e$, and plastic, $\boldsymbol{g}_t^s$, part; $\mathrm{L}_v\, \boldsymbol{t}$ stands for the Lie derivative of the tangential contact stress, ϵ_t is the tangential contact factor, f_s is the slip yield condition $\dot{\gamma}$ is the plastic multiplier and g_v is a hardening (strain-like) variable. In addition to these equations, the solution must fulfill the Kuhn-Tucker conditions. After discretizing these equations, an implicit time integration scheme is obtained formally equivalent to the well-known one-dimensional return mapping of elasto-plastic constitutive equations (Simo and Hughes, 1998).

Several slip yield conditions have been implemented in GPFEM. In the work presented here it is assumed that the clay-steel interface obeys a Coulomb law formulated in terms of the effective stress:

$$f_s(\boldsymbol{t}, \sigma'_n, g_v) = |\boldsymbol{t}| - \mu\, \sigma'_n \tag{20}$$

3. APPLICATIONS

3.1 Consolidation beneath a circular footing

The first example of application involves the computation of the loading and subsequent consolidation of a linear elastic soil by an impermeable, rough, rigid circular footing. This problem has been previously used as benchmark (Wang et al, 2015), so it allows comparison with other numerical approaches.

The example is used to explore the influence of the temporal and spatial discretizations, stress the benefits of the stabilization procedure and study the performance of the mixed formulation. To concentrate on those aspects neither the contact nor the remeshing algorithms are used in the solution. Therefore, instead of simulating the footing as a rigid body indenting the soil, the footing is discretized as a deformable but very rigid body –with elastic modulus two orders of magnitude larger than that of the soil. Load is applied on top of the footing. Additionally, and due to the relatively small displacements involved, remeshing algorithms may be disabled so that the solution is unaffected by mesh interpolation.

The analysis is set up following Wang et al. (2015). The circular footing radius and height are equal to 0.5 m. The loading boundary condition is ramped from 0 to 150 kPa in one day; afterwards it is held constant to observe consolidation. The domain is 12 radii in width and 6 radii in height. The relevant material properties are Young Modulus, E = 500 kPa, Poisson's ratio, ν = 0.3, and a permeability k = 10^{-4} m/d. As in Wang et al. (2015), we also specify unit weight γ_m = 19.6 kN/m^3 and K_0 = 0.43, although these input values do not have any effect on the output of this quasi-static elastic problem. The initial condition for water pressure is hydrostatic; drainage is only allowed at the free upper boundary.

The problem is discretized with three different meshes, progressively refined (Figure 1 and Table 1). In all of them the footing and the nearby zone have structured meshes. Element sizes at the footing are given by $h_e = 0.5R$ (MeshA), $h_e = 0.25R$ (MeshB) and $h_e = 0.125R$ (MeshC). Therefore between 3 and 9 nodes are shared by the footing and the soil. In Wang et al. (2015) an element size of *0.25R* is used but, since the elements are quadratic, the discretization level is similar to that of mesh C. A constant time-step is used during the loading phase; during the consolidation phase the time increment is updated according to $\Delta t_{n+1} = 1.05\, \Delta t_n$.

Figure 2a shows the evolution of vertical displacement at the centerline of the footing for the three grids, computed using both the primal and mixed formulations. Figure 2b presents the pore pressure evolution at depths of one, two and three radii beneath the footing centerline. Both mesh coarsening and problem formulation have a small but perceptible influence on the results: a finer mesh results in slightly larger settlements and pore pressures.

Coarser meshes hence result in a modest stiffening of the model response; the same happens when the primal (**u** - p_w) formulation is used instead of the mixed one ($\boldsymbol{u} - \theta - p_w$). Figure 3 presents these effects at the end of the loading phase, showing a linear dependency with element size. The (small) difference between mixed and primal formulation may be explained as a result of volumetric locking, which would affect the primal formulation during undrained

loading. Indeed, as shown in Figure 2, differences between primal and mixed formulation results are practically constant during the consolidation phase.

Figure 2a also includes the results reported by Wang et al. (2015) for simulations of the same problem, using RITSS and EALE. At a comparable level of discretization (mesh C), the GPFEM solution is practically coincident for the undrained phase, but a small difference appears during consolidation. Indeed, GPFEM shows a slightly stiffer response predicting a final settlement value of 0.168 m, about 96% of the value attained by Wang et al. (0.175 m).

This difference may be explained by the different variables used in the basic formulation. In GPFEM the elastic moduli relates Kirchhoff stress and Hencky (logarithmic) strain. In RITSS and EALE the modulus relates an objective rate of Cauchy stress and the rate of deformation tensor. Using identical values of elastic moduli in both formulations will not produce the same results, except at very small strains. In the problem analyzed Hencky strain levels attain peaks above 10%. Interestingly, for uniform Hencky strains of that magnitude, a one-dimensional analysis indicates that the required modulus to obtain equivalence is 95% of the small strain value.

The problem has been recomputed using a soil modulus increased 100 times to 50,000 kPa and modifying the permeability so as to maintain the same coefficient of consolidation. The increased stiffness results in strain levels well within the small strain range. A normalized settlement evolution plot (Figure 4) shows that, when small strains are guaranteed, the GPFEM computation follows quite closely the reference solution. Garino et al (2006) present other comparisons between hypoelastic and hyperelastic formulations that further clarify this effect.

Booker & Small (1986) published analytical solutions for the problem of consolidation beneath a smooth impermeable circular raft of finite stiffness. The normalized consolidation curve from that solution is compared with the numerical solutions in Figure 5. All numerical solutions plot very close to one another and the small differences with the analytical solution are likely due to the different mechanical interface condition (smooth contact vs perfect adherence). The use of stabilization in the mass conservation equation does not seem to produce any over-diffusive effect.

A separate parametric analysis was performed to examine the influence of the time step and the performance of the numerical stabilization procedure. The footing consolidation problem was thus recomputed using different time-steps, ranging from 1 day to 0.01 days. Figure 6 shows the influence of the time step size on the settlement at the end of the loading phase. For this particular mesh the stabilization term activation condition (see Equation (7)) is fulfilled when the time step falls below 0.38 days. Once stabilization is active, the slight reduction in settlement that initially accompanies time step reduction is eliminated. However, the more visible benefits of stabilization appear examining the spatial oscillations of the water pressure solution, (Figure 7) which disappear when the stabilization term is active. Although this kind of spatial oscillation may be relatively inconsequential here, that is not the case for more challenging simulations such as those considered next.

3.2 Cone penetration test: effects of permeability and interface friction

In this section, the proposed numerical technique is applied to an axisymmetric case: the Cone Penetration Test. A CPTu with standard dimensions (D = 37.5mm; apex angle 60º) is pushed into a Modified Cam Clay (MCC) soil. A parametric study is presented in which permeability and interface friction angles are varied to observe their effect on net cone resistance, sleeve friction and pore pressure generation at the three standardized measurement positions: *u1* position (at the midface of the cone), *u2* (at the apex between the cone and the shaft) and *u3* position (just above the friction sleeve, at 7.5 cone radii above the apex); the position of these measurement points is depicted in Figure 8(b).

Several researchers (Obrzud et al. 2011; Yi et al. 2012; Sheng et al. 2014) have addressed this problem using the commercial code Abaqus, although Yi et al (2012) did not use MCC, but rather a Drucker-Prager model, in which sometimes a separate volumetric hardening cap was included. A frictionless contact has been generally favoured to avoid numerical breakdowns: only Obrzud et al. (2011) report successful simulations with a frictional contact. However, they also reported numerical difficulties in that case which restricted their work to relatively small penetrations (z < 6D) and relatively low friction values (δ < 5°). Such friction values are well below those observed in steel-clay interface friction experiments, (for instance, Tsubakihara et al. 1993, report δ within a range of 22° to 27°).

Ceccato et al (2016a; 2016b) have used a code based on the material point method (MPM) to study this problem using MCC. The approach followed is powerful but computationally demanding: the code is three-dimensional and the problem is described within a fully dynamic setting, where both solid and fluid velocities (***v***-***w***) are used as primary variables to describe fluid-solid coupling. Both mass-scaling and local damping were introduced to speed-up and stabilize the semi-explicit time integration scheme.

The basic constitutive parameters used here are listed in Table 2, alongside those of previous work which is later used for comparison (unfortunately, parameters in Obrzud et al. (2011) are not clearly reported). The selected values try to mimic the example reported by Sheng et al (2014), although here the effect of the weight of the soil has been omitted and the initial effective stress and water pressure have been chosen to match those encountered in Sheng et al (2014) at final penetration depth (Table 3).

The domain (Figure 8a) has 30 times the cone radius for width and 60 times for the depth. Computation starts with the cone pre-installed at a depth of 3 cone radii. This avoids the numerical problems that may arise at the first steps of the calculation, when only a node of the soil is in contact with the rigid structure. The cone is pushed at the standard velocity (20 mm/s). Drainage is only allowed through the bottom boundary of the soil domain. A constant vertical stress is applied at the top boundary. The radial displacements are fixed on the left and right boundaries whereas null displacement in all directions is precribed at the bottom of the domain.

The simulations used $\boldsymbol{u} - \theta - p_w$ elements due to their good numerical performance for CPT simulation in undrained conditions (Monforte et al, 2017b). Good performance in this context means: smoother cone resistance curve, smaller oscillations in calculated water pressure at the measurement positions –*u1*, *u2* and *u3*- and oscillation-free stress states. Intense

remeshing takes place during cone advance (Figure 8b); despite that the final mesh typically has around 1500 elements. This final number is around one order of magnitude smaller than the number of elements employed by Ceccato et al (2016) or Sheng et al (2014). Note also that the elements are here linear triangles, instead of tetrahedra or 8-noded quadrilaterals.

Smooth interface

Figure 9 illustrates the effect of permeability on the basic cone measurements (net tip resistance, q_n and excess pore pressures at the three measurement positions). In all cases the interface soil-cone interface is perfectly smooth. It can be seen that for the highest permeability value employed (10^{-3} m/s) no excess pore pressure is generated. On the other hand, the differences in excess pore pressure for the two cases with smallest permeability values (10^{-6} m/s and 10^{-8} m/s) are minimal, so undrained conditions may be assumed for the lowest permeability case.

The profiles in Figure 9 have been filtered using a mobile average of window width 0.1R (0.2R for u_2). This smoothens numerical oscillations due to remeshing at the soil-cone interface. This filtering is very effective for the pore pressures -where the remeshing induced error is just due to a slightly variable sampling position in areas of high pressure gradients. It is somewhat less effective for the tip resistance in the stronger soils, as the remeshing induced error for that variable is mostly due to jumps in equilibrium conditions. In Table 4 the mean values at steady state (i.e. computed averaging between 15 < z/R < 25) are reported. Excess pore pressure at the *u2* position lies between 75 and 80% of that measured at the *u1* position, in good agreement with typical observations in soft low OCR soils (Lunne et al. 1997).

Undrained penetration requires less force than drained penetration. This is a well-known result that can be explored further examining, for drained and undrained conditions, total and effective stress profiles alongside the cone (Figure 10). Vertical equilibrium at the tip identifies the main cause of increased tip resistance: in drained conditions much larger tangential stress is mobilized at the tip interface (0 < z/R < 2). On the other hand, total vertical stress in that zone appears not much affected by drainage. A more distant cause can be found in the effective stress levels below and around the cone tip (say for z/R < 2). Pore pressure increases result in much smaller effective stress normal components for the undrained case; consequently mobilized strength and stiffness in that zone will be much reduced.

Following proposals by Randolph & Hope (2004) it has become customary to assess the influence of permeability on cone penetration results using normalized plots. In Figure 11 two such plots are provided, comparing the outputs of the GPFEM simulations and equivalent results obtained with ALE (Sheng et al. 2014) or MPM (Ceccato et al. 2016 a,b). The horizontal axis for both plots is the normalized velocity, defined as

$$V = \frac{vD}{c_v} = \frac{\lambda \gamma_w v D}{\sigma'_{v0} k (1+e_0)} \tag{21}$$

where v represents penetration velocity, D cone diameter and c_v is the "in situ" coefficient of consolidation. That "in situ" c_v is used only for data normalization purposes; consolidation around the cone may be governed by different values (Mahmoozadeh & Randolph, 2014) a

discussion of which is outside the scope of this work. The vertical axis in Figure 11a (q_n/q_{ref}) shows net cone tip resistance normalized by the value at the undrained limit, whereas in Figure 11b it shows the excess pore pressure at position 2, also normalized by the value at the undrained limit.

Overall, the results in Figure 11 show good agreement between the different numerical approaches. The normalized velocity transition range that appears (roughly from 0.03 to 100) fits well with that noted by De Jong & Randolph (2012) summarizing previous experimental and numerical research on soft contractive soils. Comparing with that work, it does also appear that the numerically obtained upper bound of the normalized net tip resistance ratio (q_n/q_{ref}) is somewhat low (around 1.5 here instead of 2.5 on average for De Jong & Randolph). A large part of that discrepancy may be due to interface friction.

Interface friction

The precedent CPTu analyses have been repeated using friction angles at the cone-soil interface, δ, of 10°, 20° and 25° corresponding to interface friction ratios μ betwen 0 and 0.47. Also, if we consider that the soil friction angle, ϕ_{soil}, is 25.4°, the values explored correspond to interface efficiencies (tan (δ) / tan (ϕ_{soil})) between 0 and 0.98.

Figure 12 shows the effect of this parameter for the main test results for the extreme conditions of permeability (corresponding to fully drained or undrained penetration). When cone penetration is undrained interface friction appears to have a relatively small effect on either tip resistance or pore pressure increase. When cone penetration is drained the tip resistance does increase quite significantly as friction increases.

The effect of interface friction on some aspects of the penetration mechanism is illustrated in Figure 13. One obvious difference is that friction results in significant settlement next to the cone at the upper surface. Also induced radial and vertical stress around the cone tip are significantly affected by interface friction: larger friction values increases the size of the stress bulb in front of the cone tip, which also exhibits a more vertical orientation.

A more systematic view is presented in Figure 14, showing the effect of interface friction on the relation between normalized test velocity and normalized test results. The average summary curves proposed by De Jong & Randolph (2012) are also included as reference. Again interface friction seems to have a moderate effect on pore pressure, (the somewhat erratic influence of friction at the undrained end is likely due to numerical noise). Again, the effect on normalized resistance increases as the penetration rate gets closer to drained conditions. For the upper values of interface friction the backbone curves become significantly steeper and get closer to the average reported by De Jong & Randolph (2012).

The effect of relative stiffness also plays a role here. Yi et al (2012) show that higher normalized elastic stiffness (G/p') results in an increased drained tip resistance and the backbone curve becomes steeper. The same happens when relative plastic stiffness (κ/λ) decreases (Yi et al. 2012; Sheng et al. 2014). In the GPFEM analyses presented here, the values of those parameters are kept constant at a relatively low level ($G_0/p' = 10$; $\kappa/\lambda = 0.16$). A more systematic analysis of this effect is beyond the scope of this paper.

Similar effects have been reported by Ceccato et al (2016 a,b), although the pattern of net tip resistance increase with interface friction is somewhat different to that found here (Figure 15), with stronger effects of small friction for fast penetration. The differences in the contact algorithm employed may explain this discrepancy.

Finally, as shown in Figure 12c, the mobilized stress at the friction sleeve, f_s, increases linearly with interface friction, and has a value that is practically independent of drainage conditions. This result may be related to the repeated field observation of poor repeatability on CPTu friction sleeve readings (Lunne, 2012). Although other aspects of friction sleeve design may be involved, Lunne & Andersen (2007) already pointed out at sleeve roughness as a possible contributing factor. The numerical results support that idea: poorly controlled sleeve roughness will result in significant variance on interface friction and, therefore, on f_s.

4. Conclusion

A PFEM formulation has been presented that is capable of tackling large deformation problems often encountered in geotechnical problems that involve the partially drained insertion of rigid bodies into the soil. Particular attention has been paid to the stabilization procedure, the use of a mixed formulation, the large-strain constitutive equations and the contact model.

The performance of the method is examined by reference to two examples of application. The first one involves the loading and consolidation of a poroelastic soil under a circular footing. The effect of mesh discretization and of the use of the stabilized formulation is assessed. In addition, the results show a good correspondence with those obtained using alternative numerical formulations.

The second example addresses the more challenging case of the insertion of a cone simulating the conditions of a CPTU test. It is shown that the proposed method is able to perform the numerical analysis efficiently even when significant contact friction angles are involved. Cone resistance, sleeve friction and pore pressures at three potential measurement points are obtained. The results span the full range from drained to undrained conditions and the effect of the contact friction can be readily explored throughout. The numerical results also allow a better understanding of the mechanisms underlying CPTu observations under different conditions. The PFEM method, therefore, provides a very promising and effective procedure for the analysis of large-deformations coupled geotechnical problems provided the enhancements described in this paper are incorporated.

In this respect it is worth noting that several applications of the methodology here described are currently being developed: enhanced interpretation of CPTu in complex soils, like lacustrine varved clays (Hauser, 2017); systematic examination of current procedures for permeability identification using CPTu (Monforte et al. 2018a); evaluation of specific recovery ratio during quasi-static sampling (Monforte et al., 2017c). Those applications are simultaneous with further developments of the GPFEM platform, like element technology for three-dimensional cases (Monforte et al. 2018b) or a full-Biot formulations (Navas et al, 2017a,b) for impact problems. New developments like these would allow to address more challenging problems within the area of soil investigation, such as DMT insertion, dynamic driving or impact coring. A medium term goal is to use GPFEM as a unique simulation platform

in which both site investigation and foundation installation can be treated, thus facilitating the always complex connection between in situ testing and geotechnical design.

Acknowledgments

The financial support of the ministry of Education of Spain through research grant BIA2014-59467-R is gratefully appreciated.

5. Appendix A: auxiliary formulation

The expression for the matrices used in the discretized expression of the governing equation of the problem are

$$\boldsymbol{P}(\boldsymbol{\sigma}) = \int_{\Omega_t} \boldsymbol{B}^T \cdot \boldsymbol{\sigma} \, \mathrm{d}\Omega_t$$

$$\boldsymbol{f}^{ext} = \int_{\Gamma_{\bar{\boldsymbol{t}}}} \boldsymbol{N}_u^T \cdot \boldsymbol{t} \, \mathrm{d}\gamma \; + \int_{\Omega_t} \boldsymbol{N}_u^T \, \rho \cdot \boldsymbol{g} \, \mathrm{d}\Omega_t$$

$$\boldsymbol{Q} = \int_{\Omega_t} \boldsymbol{B}^T \cdot 1 \cdot \boldsymbol{N} \, \mathrm{d}\Omega_t$$

$$\boldsymbol{Q}^* = \int_{\Omega_t} \boldsymbol{B}^T \cdot 1 \cdot \boldsymbol{N} \left(\frac{1}{J}\right) \mathrm{d}\Omega_t$$

$$\boldsymbol{M} = \int_{\Omega_t} \boldsymbol{N}^T \cdot \boldsymbol{N} \, \mathrm{d}\Omega_t$$

$$\boldsymbol{H} = \int_{\Omega_t} \nabla \boldsymbol{N} \cdot \boldsymbol{k} \cdot \nabla \boldsymbol{N} \left(\frac{1}{J}\right) \mathrm{d}\Omega_t$$

$$\boldsymbol{f}^{pw} = \int_{\Gamma_{\bar{j}}} \boldsymbol{N}^T \cdot \bar{j} \, \mathrm{d}\gamma - \int_{\Omega_t} \nabla \boldsymbol{N}^T \cdot \boldsymbol{k} \cdot \boldsymbol{g} \left(\frac{\rho_w}{J}\right) \mathrm{d}\Omega_t$$

6. Appendix B: notation

$\boldsymbol{B}$	Strain-displacement finite element matrix
c_v	Coefficient of consolidation
C_c	Contact contribution
D	Cone diameter
e_0	Initial void ratio
E	Young modulus
$\boldsymbol{F}$	Deformation gradient
$\breve{\boldsymbol{F}}$	Assumed deformation gradient
f_s	Slip yield condition
$\boldsymbol{f}^{ext}$	Mechanical external forces

$\boldsymbol{f}^{pw}$	Hydraulic external forces
f_s	Friction sleeve resistance
$\boldsymbol{g}$	Gravity vector
G	Shear modulus
G_0	Parameter of the Houlsby hyperelastic model
g_n^-	Penetration function
$\boldsymbol{g}_t$	Tangential gap
$\boldsymbol{g}^e{}_t$	Elastic tangential gap
$\boldsymbol{g}_t^s$	Plastic tangential gap
g_v	Hardening variable (strain-like)
$\boldsymbol{H}$	Finite element hydraulic conductivity matrix
h_e	Element size
$\boldsymbol{I}^d$	Fourth order deviatoric tensor
J_2	Second invariant of the deviatoric stress
$J = \det(\boldsymbol{F})$	Jacobian
j	Imposed water flux at Neumann
$\boldsymbol{k}, k$	Permeability tensor, permeability (scalar)
K_w	Water bulk modulus
K	Volumetric modulus
K_0	Coefficient of lateral earth pressure
L_v	Lie derivative
M	Constrained modulus
M	Critical state line
$\boldsymbol{M}$	Finite element mass matrix
$\boldsymbol{N}$	Shape functions of scalar fields
$\boldsymbol{N\_u}$	Shape functions of the displacement field
$\boldsymbol{N}$	Outward normal
$\boldsymbol{P}(\boldsymbol{\sigma})$	Internal forces due to $\boldsymbol{\sigma}$
p_0	Reference pressure (Houlsby hyperelastic model)
p_c	Preconsolidation pressure
p_{c0}	Initial presconsolidation pressure
p_w	Water pressure
p_{w0}	Initial water pressure
$\overline{p_w}$	Water pressure at the dirichlet boundary
$\boldsymbol{Q}$	Finite element coupling matrix
$\boldsymbol{Q}^*$	Finite element coupling matrix
Q	Virtual water pressure
q_n	Net cone resistance
R	Radii of the footing. Radii of the CPT.
t	Time
$\boldsymbol{t}$	Tangential contact stress
U	Degree of consolidation settlement
$\boldsymbol{u}$	Solid skeleton displacement
$\boldsymbol{u}_0$	Initial solid skeleton displacement
$\overline{\boldsymbol{u}}$	Prescribed solid skeleeton displacement
$\boldsymbol{u}^h$	Discretized solid skeleton displacement field
$\widetilde{\boldsymbol{u}}$	Nodal solid skeleton displacement
V	Normalized CPT velocity
V	Generic internal variables of the constitutive model
v	Cone velocity

$\boldsymbol{v}$	Solid skeleton velocity
$\boldsymbol{v}^d$	Darcy's velocity
$\boldsymbol{w}$	Virtual displacement
$\boldsymbol{x}$	Position at the deformed configuration
$\boldsymbol{X}$	Position at the reference configuration
$\boldsymbol{1}$	Second order identity tensor
α	Parameter of the Houlsby hyperelastic model
Δt	Time-step
δ	Interface friction angle
δ_{ij}	Kronecker delta
γ	Plastic multiplier
γ_m	Mixture specific weight
$\Gamma_{\bar{\boldsymbol{u}}}$	Boundary with prescribed displacement
$\Gamma_{\bar{p}}$	Boundary with prescribed water pressure
$\Gamma_{\bar{\boldsymbol{t}}}$	Boundary with prescribed traction
$\Gamma_{\bar{j}}$	Boundary with prescribed water flux
Γ_c	Boundary in contact
ϵ	Penalty factor
ϵ_t	Tangential penalty factor
$\boldsymbol{\varepsilon}_d^e$	Elastic deviatoric hencky strain
ε_v^e	Elastic volumetric hencky strain
$\boldsymbol{\varepsilon}^e$	Elastic Hencky strain
ε_v^p	Plastic volumetric Hencky strain
θ	Assumed jacobian
θ_L	Lode's angle
κ^*	$\dfrac{\kappa}{(1+e_0)}$
κ	Swelling slope
λ^*	$\dfrac{\lambda}{(1+e_0)}$
λ	Slope of the virgin consolidation line
μ	$\tan(\delta)$ Interface friction ratio
ν	Poisson's ratio
π'	Effective Kirchhoff mean stress
ρ_m	Mixture density
ρ_m^0	Initial mixture density
ρ_s	Solid phase density
ρ_w	Water density
$\boldsymbol{\sigma}$	Cauchy total stress
$\boldsymbol{\sigma}'$	Cauchy effective stress
σ_n	Normal total contact stress
σ_n'	Normal effective contact stress
σ_{v0}'	Initial vertical Cauchy effective stress
τ	Stabilization parameter
$\boldsymbol{\tau}'$	Kirchhoff effective stress
τ_{rz}	Deviatoric stress component of the Cauchy stress tensor.
ϕ	Soil friction angle

φ	Soil porosity
φ_0	Initial soil porosity
ψ	Stored energy function
Ω_0	Reference domain
Ω_t	Deformed domain at time *t*

7. References

Arroyo, M., Butlanska, J., Gens, A., Calvetti, F., & Jamiolkowski, M. (2011). Cone penetration tests in a virtual calibration chamber. Géotechnique, 61(6), 525-531.

Bochev, P. B., Dohrmann, C. R., & Gunzburger, M. D. (2006). Stabilization of low-order mixed finite elements for the Stokes equations. *SIAM Journal on Numerical Analysis*, *44*(1), 82-101.

Booker, J. R., & Small, J. C. (1986). The behaviour of an impermeable flexible raft on a deep layer of consolidating soil. International Journal for Numerical and Analytical Methods in Geomechanics, 10(3), 311-327.

Borja, R. I. and E. Alarcón (1995). A mathematical framework for finite strain elastoplastic consolidation part 1: Balance laws, variational formulation, and linearization. Computer Methods in Applied Mechanics and Engineering 122 (1-2), 145-171

Borja, R.I., Tamagnini, C. and Amorosi, A. (1997) Coupling plasticity and energy-conserving elasticity models for clays. Journal of Geotechnical and Geoenvironmental Engineering. 123(10):948-957.

Carbonell, J., Oñate, E., and Suárez, B. (2010) ”Modeling of Ground Excavation with the Particle Finite-Element Method.” ASCE J. Eng. Mech., 136(4), 455–463.

Carbonell, J. M., Oñate, E., & Suárez, B. (2013) Modelling of tunnelling processes and rock cutting tool wear with the particle finite element method, Computational Mechanics, 52(3), 607-629

Carter, J. P., J. R. Booker, and J. C. Small (1979). The analysis of finite elasto-plastic consolidation. International Journal for Numerical and Analytical Methods in Geomechanics 3 (2), 107-129

Chapuis, R. P. and M. Aubertin (2003). On the use of the Kozeny Carman equation to predict the hydraulic conductivity of soils. Canadian Geotechnical Journal 40 (3), 616-628.

Ceccato, F., Beuth, L., Vermeer, P. A., & Simonini, P. (2016a). Two-phase material point method applied to the study of cone penetration. Computers and Geotechnics, 80, 440-452.

Ceccato, F., Beuth, L., & Simonini, P. (2016b). Analysis of piezocone penetration under different drainage conditions with the two-phase material point method. Journal of Geotechnical and Geoenvironmental Engineering, 142(12), 04016066.

Ciantia, M. O., Arroyo, M., Butlanska, J., & Gens, A. (2016). DEM modelling of cone penetration tests in a double-porosity crushable granular material. Computers and Geotechnics, 73, 109-127.

Cui, W, Gawecka, K. A., Taborda, D.M. Potts, D.M. Zdravkovic, L. (2016) Time-step constraints in transient coupled finite element analysis. International Journal of Numerical methods in Engineering 106:953-971.

Dadvand, P., Rossi, R., & Oñate, E. (2010). An object-oriented environment for developing finite element codes for multi-disciplinary applications. Archives of computational methods in engineering, 17(3), 253-297.

De Borst, R., & Vermeer, P. A. (1984). Possibilites and limitations of finite elements for limit analysis. Geotechnique, 34(2), 199-210.

DeJong, J. T., & Randolph, M. (2012). Influence of partial consolidation during cone penetration on estimated soil behavior type and pore pressure dissipation measurements. *Journal of Geotechnical and Geoenvironmental Engineering*, *138*(7), 777-788.

Donea, J., Huerta, A., Ponthot, J. P., & Rodriguez-Ferran, A. (2004). "Arbitrary Lagrangian–Eulerian Methods" Chapter 14 in Encyclopedia of computational mechanics, Stein,E., De Borst, R. & Hughes, T.J.R. Eds., John Wiley

Garino, C., Ponthot, J. P., Mirasso, A., Koeune, R., Jeunechamps, P. P., & Cargelio, C. (2006). Numerical simulation of large strain rate dependent J2 problems. *Mecánica Computacional*, *25*, 1927-1946.

Gens, A., Arroyo, M., Butlanska, J., Carbonell, J.M., Ciantia, M., Monforte, L. & O'Sullivan, C. (2016) Simulation of the cone penetration test: Discrete and continuum approaches. *Australian Geomechanics Journal*, 51 (4), pp. 169-182

Hauser, L. (2017) Numerical simulation of cone penetration tests using G-PFEM, MSc thesis, Technischen Universitat Graz

Houlsby, G. T., Amorosi, A. Rojas, E. (2005) Elastic moduli of soils dependent on pressure: a hyperelastic formulation. Geotechnique, 55:5, pp 383-392

Houlsby, G. T. The use of a variable shear modulus in elastic-plastic models for clays. Computers and Geotehcnics 1(1), 3-13 (1985)

Hu, Y., Randolph, M.F. (1998) H-adaptive FE analysis of elasto-plastic non-homogeneous soil with large deformation. *Computers and Geotechnics*, 23 (1-2), pp. 61-83.

Larsson, J. and R. Larsson (2002). Non-linear analysis of nearly saturated porous media: theoretical and numerical formulation. Computer methods in applied mechanics and engineering 191 (36), 3885-3907.

Lunne, T., Robertson, P. K., & Powell, J. J. (1997). Cone penetration testing in geotechnical practice, New York: Blackie Academic

Lunne, T., & Andersen, K. H. (2007). Soft clay shear strength parameters for deepwater geotechnical design. In OFFSHORE SITE INVESTIGATION AND GEOTECHNICS, Confronting New Challenges and Sharing Knowledge. Society of Underwater Technology.

Lunne, T. (2012) The Fourth James K. Mitchell Lecture: The CPT in offshore soil investigations - a historic perspective, Geomechanics and Geoengineering, 7:2,75-101, DOI: 10.1080/17486025.2011.640712

Mahmoodzadeh, H., Randolph, M. F., & Wang, D. (2014). Numerical simulation of piezocone dissipation test in clays. Géotechnique, 64(8), 657-666.

Mayne, P. W. (2007). Cone penetration testing (Vol. 368). Transportation Research Board.

Monforte, L, Arroyo, M. Gens, A & Carbonell, J.M. (2014) Explicit finite deformation stress integration of the elasto-plastic constitutive equations. Computer Methods and Recend Advances in Geomechanics – Proceedings of the 14th Int. Conference of IACMAG

Monforte, L., Arroyo, M., Carbonell, J. M., & Gens, A. (2017a). Numerical simulation of undrained insertion problems in geotechnical engineering with the particle finite element method (PFEM). Computers and Geotechnics, 82, 144-156.

Monforte, L., Carbonell, J.M., Arroyo, M., Gens, A. (2015) Numerical simulation of penetration problems in geotechnical engineering with the particle finite element method (PFEM). *Proceedings of the 4th International Conference on Particle-Based Methods - Fundamentals and Applications, PARTICLES 2015,* pp. 1073-1080.

Monforte, L., Carbonell, J. M., Arroyo, M., & Gens, A. (2017b). Performance of mixed formulations for the particle finite element method in soil mechanics problems. Computational Particle Mechanics, 4(3):269-284.

Monforte, L., Arroyo, M., Carbonell, J. M., & Gens, A. (2017c) G-PFEM: a Particle Finite Element Method platform for geotechnical applications. ALERT Geomaterials Workshop 2018.

Monforte, L., Arroyo, M., Gens, A. & Parolini, C. (2018a) Permeability estimates from CPTu: a numerical study. CPT18 - 4th International Symposium on Cone Penetration Testing.

Monforte, L., Arroyo, M., Gens, A. & Carbonell, J.M. (2018b) Three-dimensional analysis of penetration problems using G-PFEM. NUMGE-2018 - 9th European Conference on Numerical Methods in Geotechnical Engineering

Navas, P., Sanavia, L., López-Querol, S. & Rena, C.Y. (2017a) u-w formulation for dynamic problems in large deformation regime solved through an implicit meshfree scheme. https://doi.org/10.1007/s00466-017-1524-y

Navas, P., Sanavia, L., López-Querol, S. & Rena, C.Y. (2017b) Explicit meshfree solution for large deformation dynamic problems in saturated porous media. Acta geotechnical https://doi.org/10.1007/s11440-017-0612-7

Nazem, M., D. Sheng, and J. P. Carter (2006). Stress integration and mesh refinement for large deformation in geomechanics. International Journal for Numerical Methods in Engineering 65 (7), 1002–1027

Obrzud, R. F., Truty, A., & Vulliet, L. (2011). Numerical modeling and neural networks to identify model parameters from piezocone tests: I. FEM analysis of penetration in two-phase continuum. International Journal for Numerical and Analytical Methods in Geomechanics, 35(16), 1703-1730.

Oñate, E., Idelsohn, S. R., Celigueta, M. A., Rossi, R., Marti, J., Carbonell, J. M., Ryzakov, P. & Suárez, B. (2011). Advances in the particle finite element method (PFEM) for solving coupled problems in engineering. In Particle-Based Methods (pp. 1-49). Springer Netherlands.

Oñate, E., Idelsohn, S. R., Del Pin, F., & Aubry, R. (2004). The particle finite element method—an overview. International Journal of Computational Methods,1(02), 267-307

Panteghini, A. and Lagioia, R. (2014), A fully convex reformulation of the original Matsuoka–Nakai failure criterion and its implicit numerically efficient integration algorithm. Int. J. Numer. Anal. Meth. Geomech., 38: 593–614. doi:10.1002/nag.2228

Pastor, M., Li, T., Liu, X., & Zienkiewicz, O. C. (1999). Stabilized low-order finite elements for failure and localization problems in undrained soils and foundations. Computer Methods in Applied Mechanics and Engineering, 174(1-2), 219-234.

Randolph, M. F., & Hope, S. (2004). Effect of cone velocity on cone resistance and excess pore pressures. In Proc., Int. Symp. on Engineering Practice and Performance of Soft Deposits (pp. 147-152). Yodagawa Kogisha Co., Ltd..

Robertson, P. K., & Cabal, K. L. (2015). Guide to cone penetration testing for geotechnical engineering. 6th Edition. Gregg Drilling and Testing Inc., USA.

Rodriguez, J. M., Carbonell, J. M., Cante, J. C., & Oliver, J. (2016). The particle finite element method (PFEM) in thermo-mechanical problems. International Journal for Numerical Methods in Engineering, 107(9), 733-785.

Salazar, F., J. Irazábal, A. Larese, and E. Oñate (2016). Numerical modelling of landslide-generated waves with the particle finite element method (PFEM) and a non-Newtonian flow model. International Journal for Numerical and Analytical Methods in Geomechanics 40 (6), 809–826

Schnaid, F. (2009). In situ testing in geomechanics: the main tests. CRC Press.

Simo, J.C. Hughes, TJR. Computational Inelasticity, Springer-Verlag, New York, 1998

Sloan, S.W. Aboo, A.J, Sheng, D. (2001) Refined explicit integration of elastoplastic models with automatic error control. Engineering Computations, 18(1/2) 121-194

Sołowski, W. T. and S. W. Sloan (2015). Evaluation of material point method for use in geotechnics. International Journal for Numerical and Analytical Methods in Geomechanics 39 (7), 685–701

Sheng, D. Kelly, R. Pineda, J. Bates, L. (2014) Numerical study of rate effects in cone penetration test. 3rd international symposium on Cone Penetration Testing

Sun, W, Ostien, J.T & Salinger, A. G. (2013). A stabilized assumed deformation gradient finite element formulation for strongly coupled poromechanical simulations at finite strains. International Journal for numerical and analytical methods in geomechanics. 37:2755-2788.

Tsubakihara, Y., Kishida, H., & Nishiyama, T. (1993). Friction between cohesive soils and steel. Soils and Foundations, 33(2), 145-156.

Wang, D., Bienen, B., Nazem, M., Tian, Y., Zheng, J., Pucker, T. & Randolph, M. F. (2015). Large deformation finite element analyses in geotechnical engineering. Computers and Geotechnics, 65, 100-114.

Wriggers, P. (1995) Finite element algorithms for contact problems. Archives of Computational Methods in Engineering, 2(4), 1-49.

Wriggers, P. (2006). Computational contact mechanics (Vol. 30167). T. A. Laursen (Ed.). Berlin: Springer.

Yi, J. T., Goh, S. H., Lee, F. H., & Randolph, M. F. (2012). A numerical study of cone penetration in fine-grained soils allowing for consolidation effects. Géotechnique, 62(8), 707.

Yu, H. S. and J. K. Mitchell (1998). Analysis of cone resistance: review of methods. Journal of Geotechnical and Geoenvironmental Engineering 124 (2), 140–149

Zhang, X., Krabbenhoft, K., Pedroso, D. M., Lyamin, A. V., Sheng, D., Da Silva, M. V., & Wang, D. (2013). Particle finite element analysis of large deformation and granular flow problems. Computers and Geotechnics, 54, 133-142

Zhang, X., Sheng, D., Sloan, S. W., & Bleyer, J. (2017). Lagrangian modelling of large deformation induced by progressive failure of sensitive clays with elastoviscoplasticity. International Journal for Numerical Methods in Engineering.

Zienkiewicz, O. C., Chang, C. T., & Bettess, P. (1980). Drained, undrained, consolidating and dynamic behaviour assumptions in soils. *Geotechnique*, *30*(4), 385-395.

Zienkiewicz, O. C. & Taylor, R. L. (2005) The finite element method for solid and structural mechanics. Butterworth-Heinemann.

8. Tables

Table 1 Finite element meshes of the circular footing example

	Number of nodes	Number of elements
A	352	636
B	902	1712
C	3203	6236

Table 2 Constitutive parameters of Modified Cam Clay CPTu coupled analyses

Ref.	e_0	κ	λ	M	p_c (kPa)	OCR	α	G_0 (kPa)	υ	k (m/s)
This work	2.0	0.05	0.3	1	70	1.2	23.5	400	-	$10^{-3} - 10^{-8}$
Sheng et al. (2014) [z/D=40]	2.0	0.05	0.3	1		1.21	-	-	0.33	$10^{-3} - 10^{-10}$
Ceccato et al. (2016a; 2016b)	1.41	0.04	0.2	0.92		1	-	-	0.25	$1.2 \cdot 10^{-2}$ $- 2.4 \cdot 10^{-8}$

Table 3: In situ stress state for the Modified Cam Clay CPTu coupled analyses

Ref.	σ'_{v0} (kPa)	σ'_{h0} (kPa)	K_0
This work	57.85	28.93	0.5
Sheng et al. (2014) [z/D 40]	57.85	28.93	0.5
Ceccato et al. (2016a; 2016b)	50	34	0.68

Table 4: CPTu simulations: average values at steady state

δ (º)	k (m/s)	q_n (kPa)	Δu1 (kPa)	Δu2 (kPa)	Δu3 (kPa)	fs (kPa)
0	1.00E-08	155.9247	149.1725	116.8521	47.8765	0
0	1.00E-07	157.9149	145.3006	116.7007	50.2512	0
0	1.00E-06	171.913	139.035	113.8241	40.9969	0
0	5.00E-06	188	91.9542	71.1219	21.9292	0
0	1.00E-05	193.4498	62.1941	46.4524	14.5118	0
0	5.00E-05	225.2794	14.7636	11.6343	5.1592	0
0	1.00E-04	228.8778	7.7077	6.2003	2.9622	0
0	1.00E-03	228.4996	0.82064	0.64933	0.30679	0
10	1.00E-08	168.6917	147.332	113.8916	42.6165	10.0502
10	1.00E-07	170.7917	147.6641	102.8217	44.4423	9.2191
10	1.00E-06	198.016	139.1674	101.2809	38.8121	9.2646
10	5.00E-06	228.9542	97.5366	65.5577	21.9336	7.4521
10	1.00E-04	306.4265	7.9372	5.7246	2.9266	8.6699
10	1.00E-03	311.473	0.77502	0.60076	0.33279	8.8945
20	1.00E-08	178.4367	156.3127	111.0797	29.9754	19.8684
20	1.00E-07	175.4394	150.6554	86.8759	42.9122	16.8615
20	1.00E-06	206.5035	151.232	86.4064	32.8562	17.6686
20	5.00E-06	257.1764	115.4293	65.527	21.3735	17.351
20	1.00E-04	371.8288	7.8541	5.2757	3.6126	18.7267
20	1.00E-03	381.3202	0.77079	0.56783	0.40083	17.2323
25	1.00E-08	183.2952	164.3057	97.4744	24.6536	23.5184
25	1.00E-07	179.5185	152.5107	88.0873	41.5211	20.9896
25	1.00E-06	209.2947	154.2808	90.8293	34.1315	22.132

25	5.00E-06	285.1025	115.1756	57.3074	19.052	20.6526

9. Figures

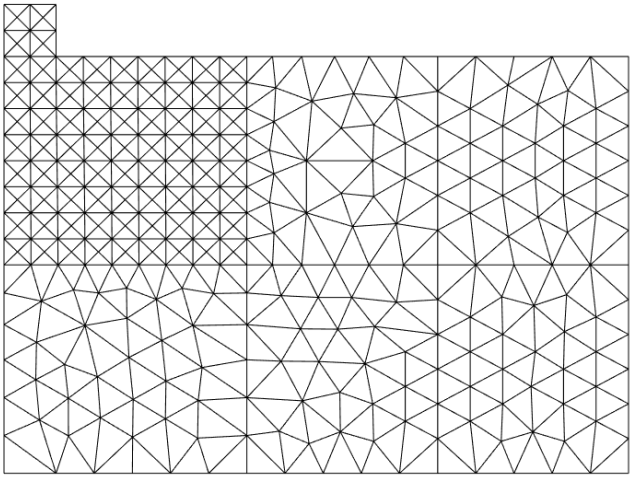

(a)

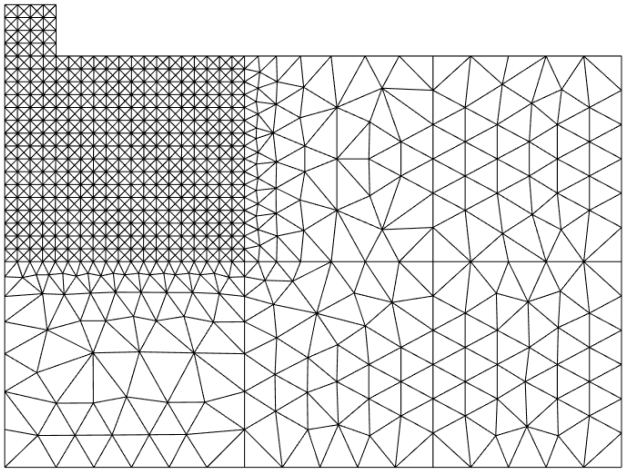

(b)

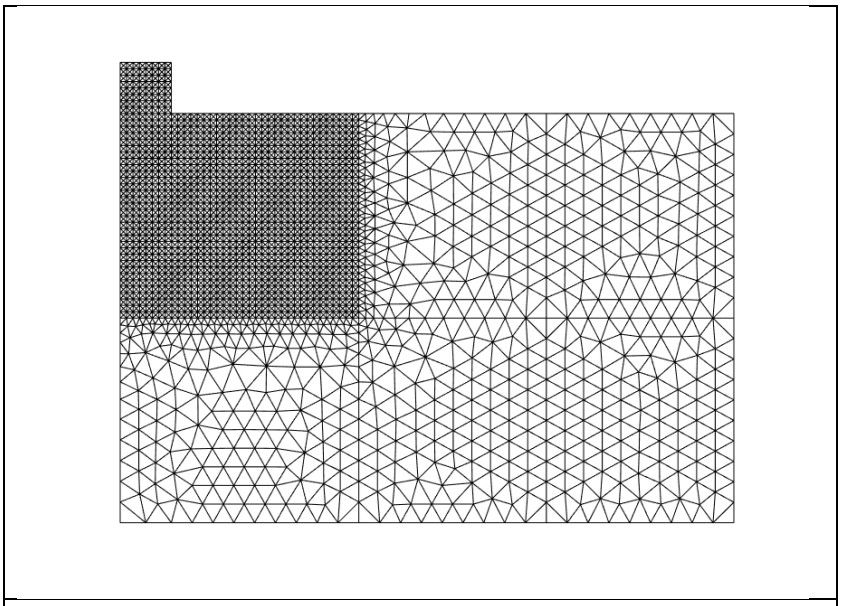

(c)

Figure 1 Rigid circular footing: Finite element meshes (a) $h_e = 0.5R$ (b) $h_e = 0.25R$ (c) $h_e = 0.125R$

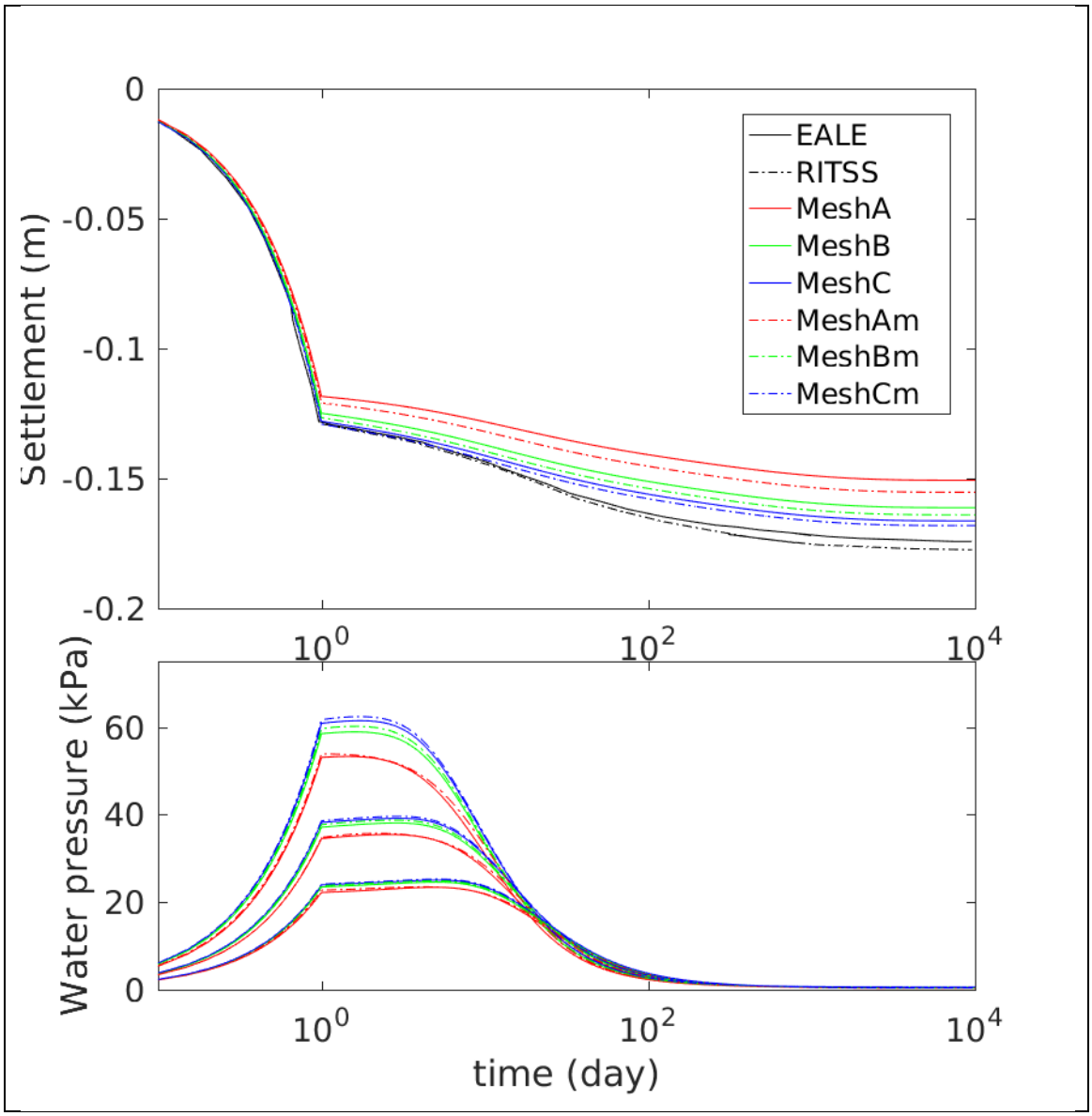

Figure 2 Rigid circular footing. Effects of mesh refinement and mixed formulation (m). Evolution of the settlements at the footing centerline (a) and water pressures at depths of one, two and three radii below the footing centerline (b).

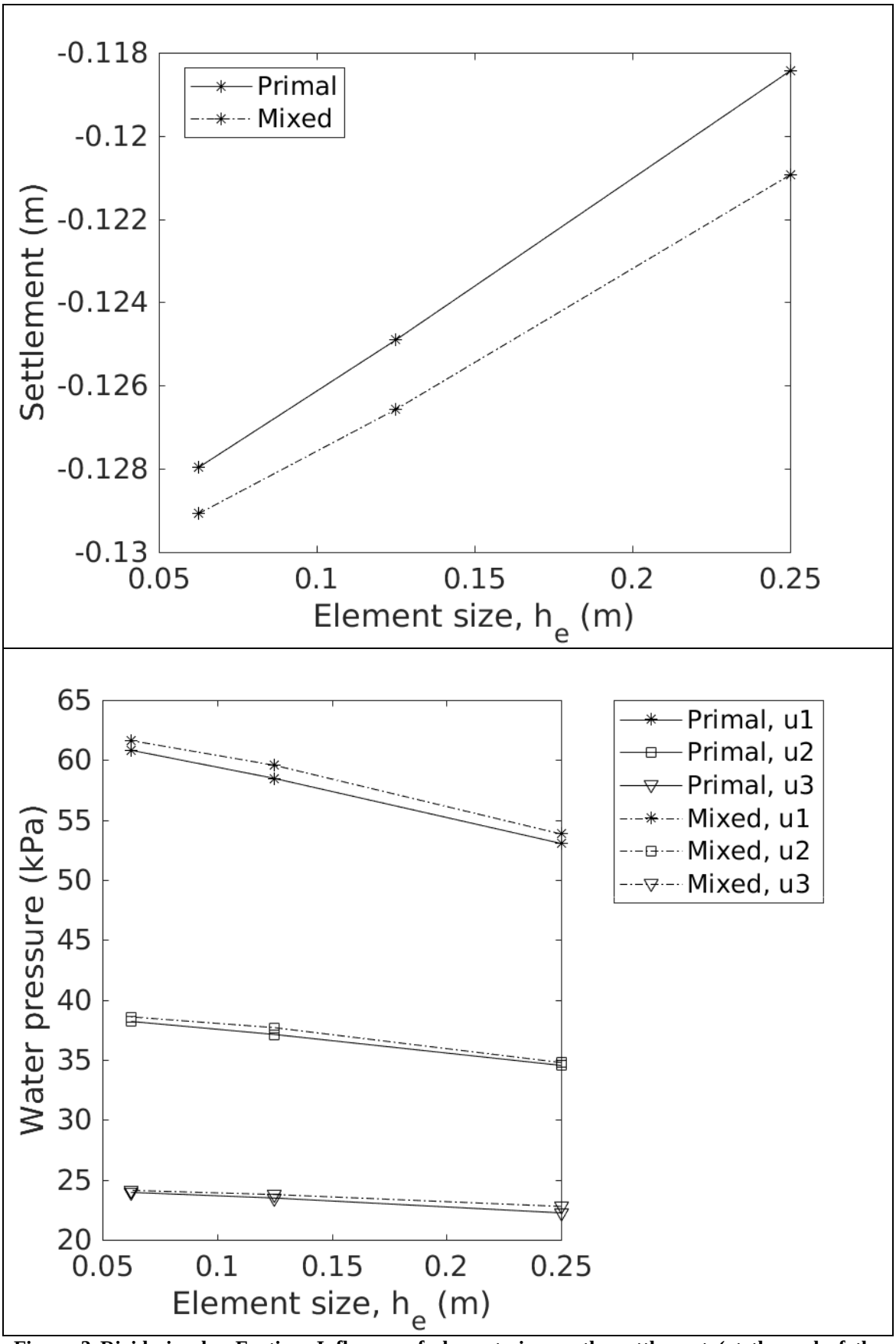

Figure 3 Rigid circular Footing. Influence of element size on the settlement (at the end of the loading phase) and excess water pressure (at the end of the loading phase) for the primal and mixed formulations. [Δt= 0.02 day]

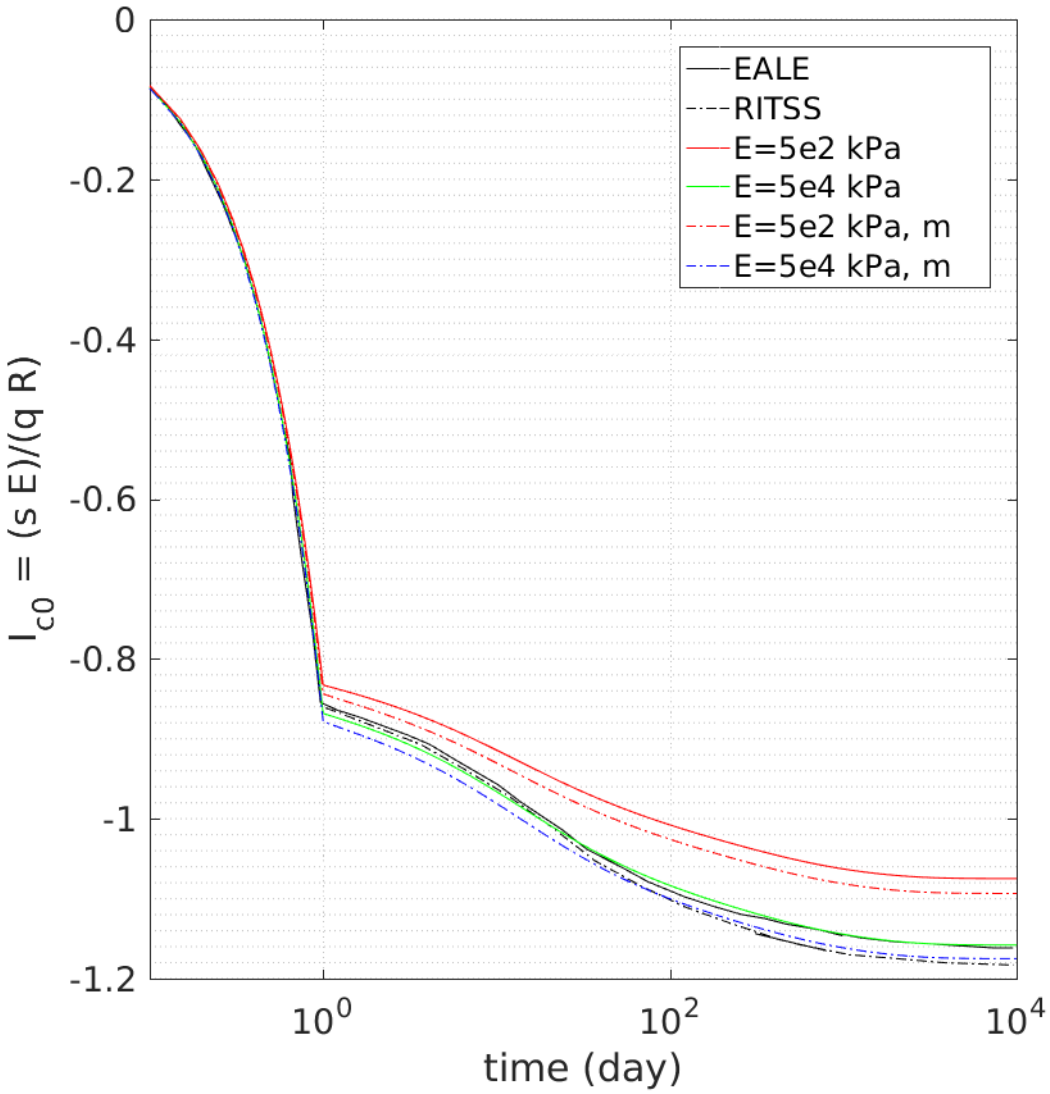

Figure 4 Rigid circular Footing. Normalized settlement evolution for high and low moduli values.

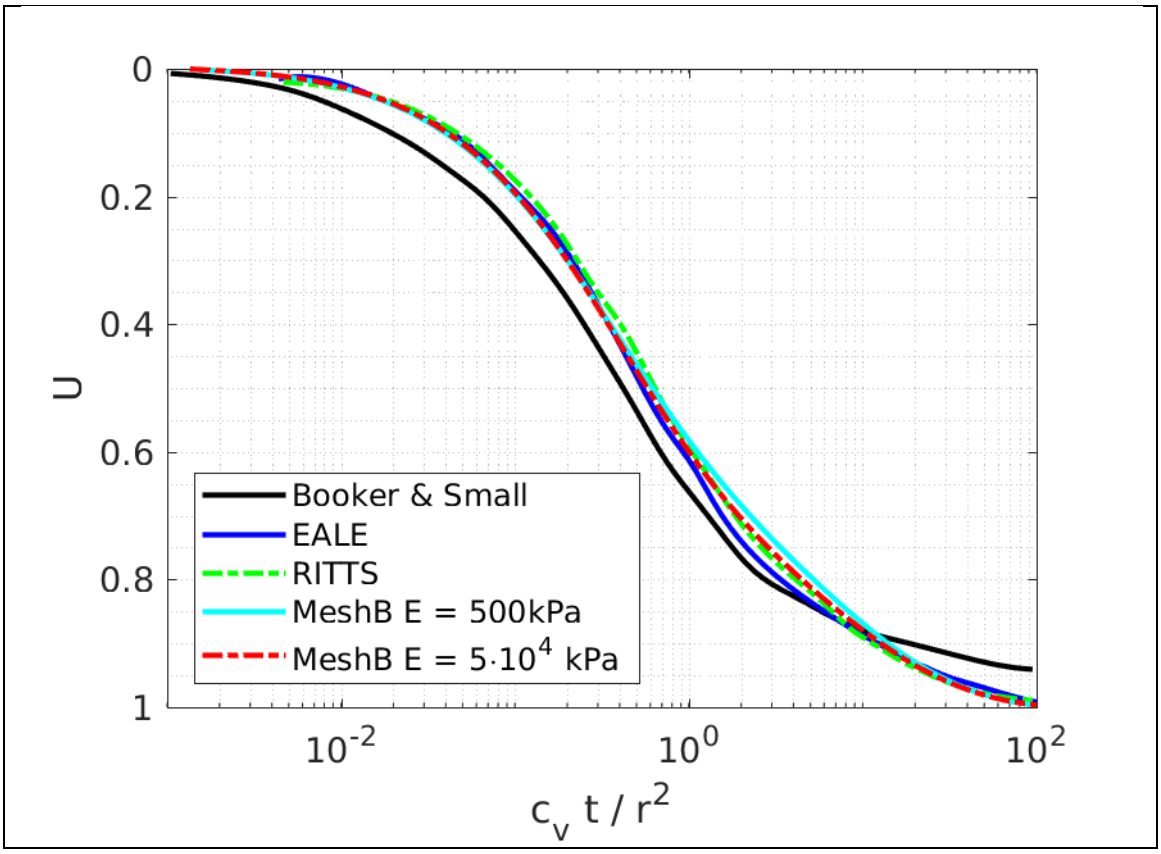

Figure 5 Rigid circular footing. Normalized settlement below the footing during the consolidation phase

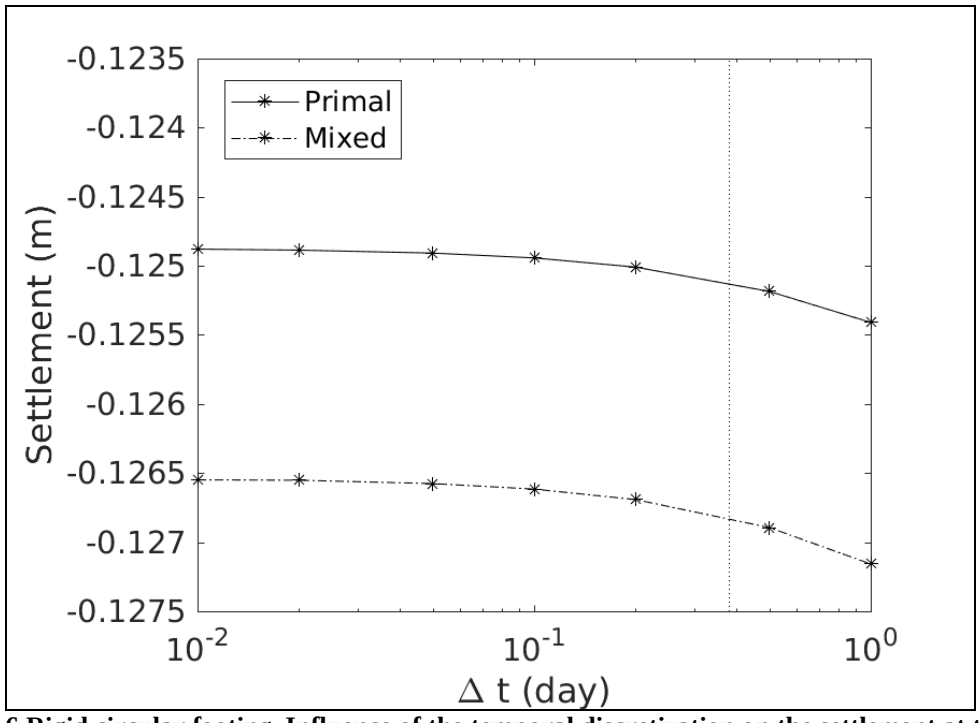

Figure 6 Rigid circular footing. Influence of the temporal discretization on the settlement at the end of the loading phase for the primal and mixed formulation. The vertical dotted line separates simulations that have elements whose stabilization parameter is larger than zero from those that all elements have a null stabilization parameter [Mesh B]

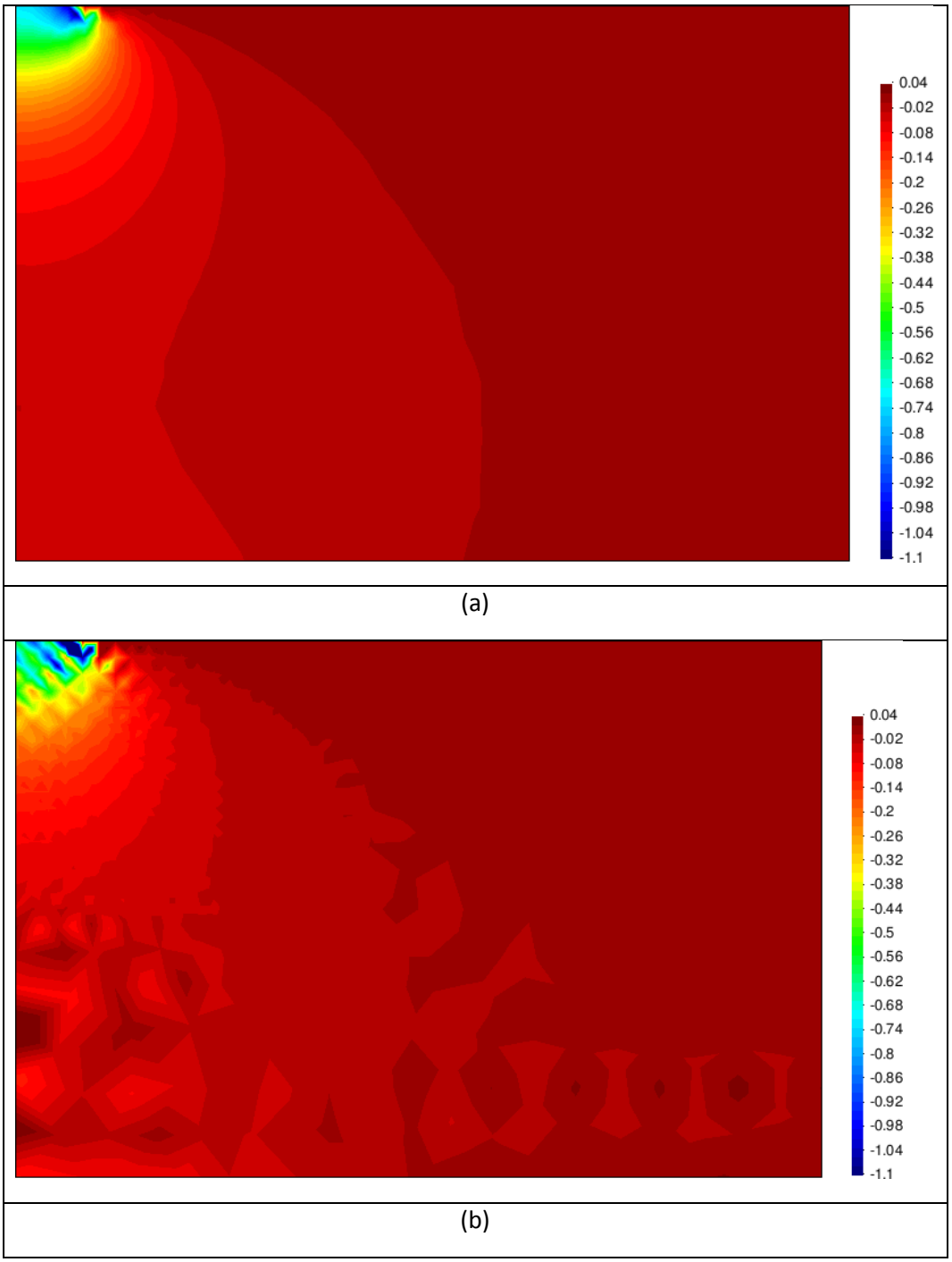

Figure 7 Excess water pressure at t = 0.01 days using mesh C. Δt = 0.01 day. On top, stabilized solution, on the bottom, unstabilized solution.

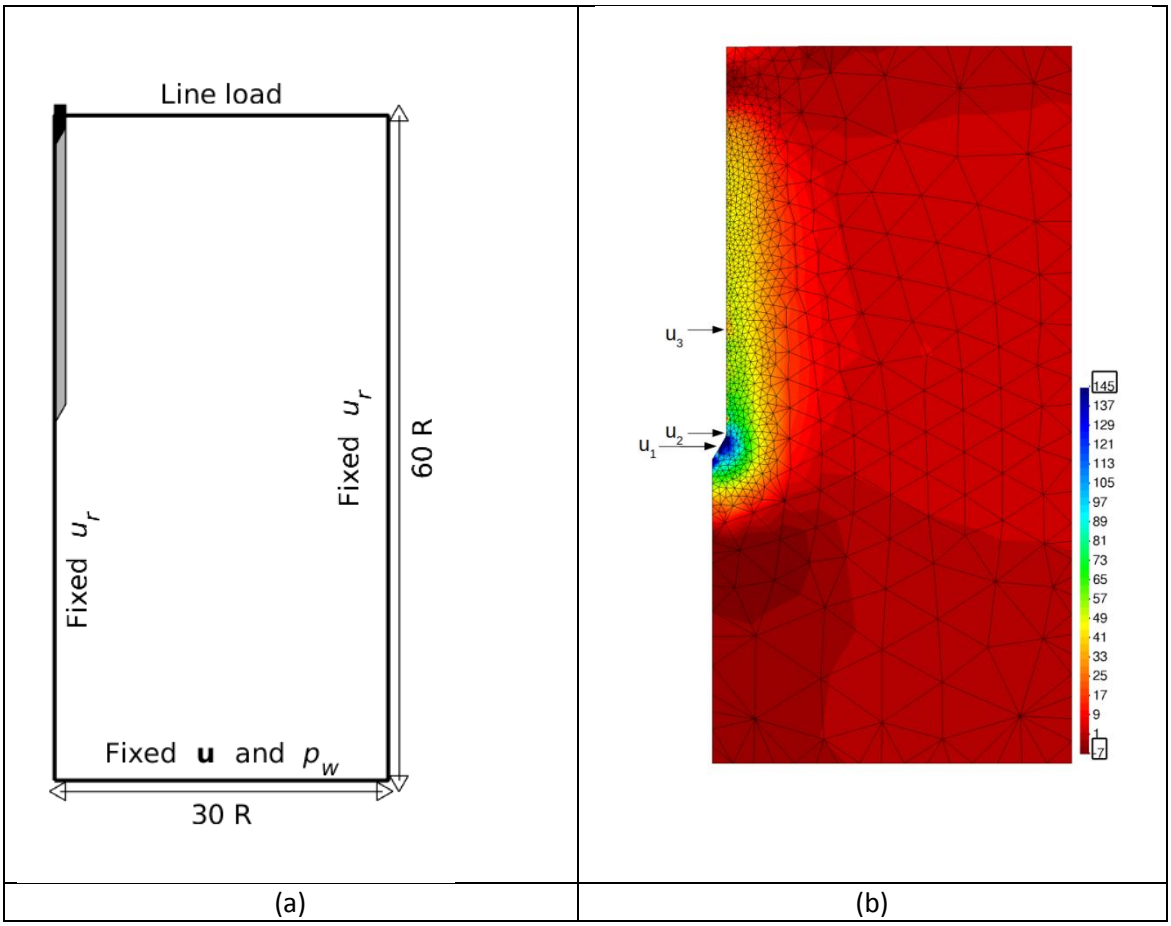

Figure 8 CPTu penetration. (a) sketch of geometrical and boundary conditions (b) mesh after 20 radius penetration

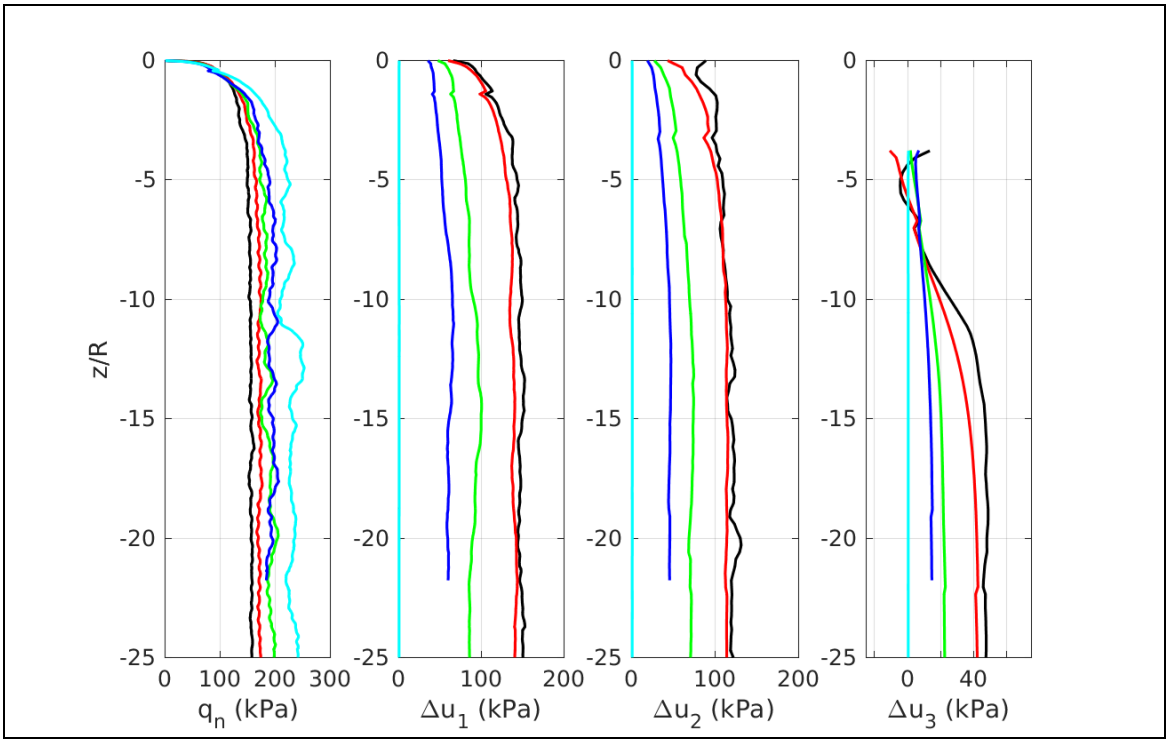

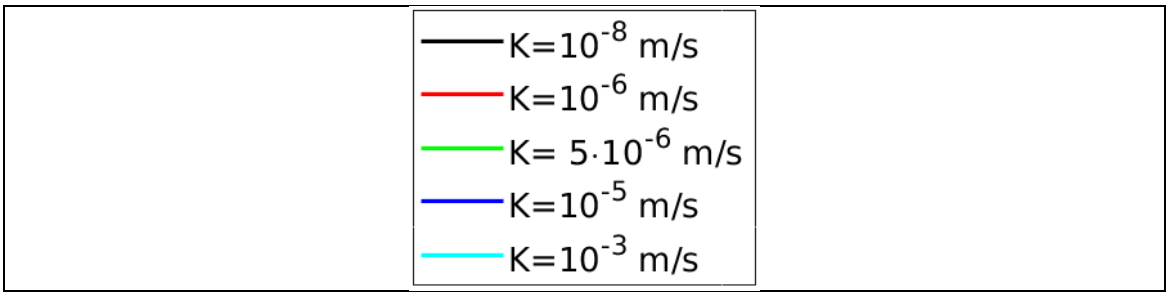

Figure 9 Cone penetration test. Profiles of net cone resistance and water pressure at the three measurement positions vs normalized penetration depth. Smooth interface with Ko = 0.5

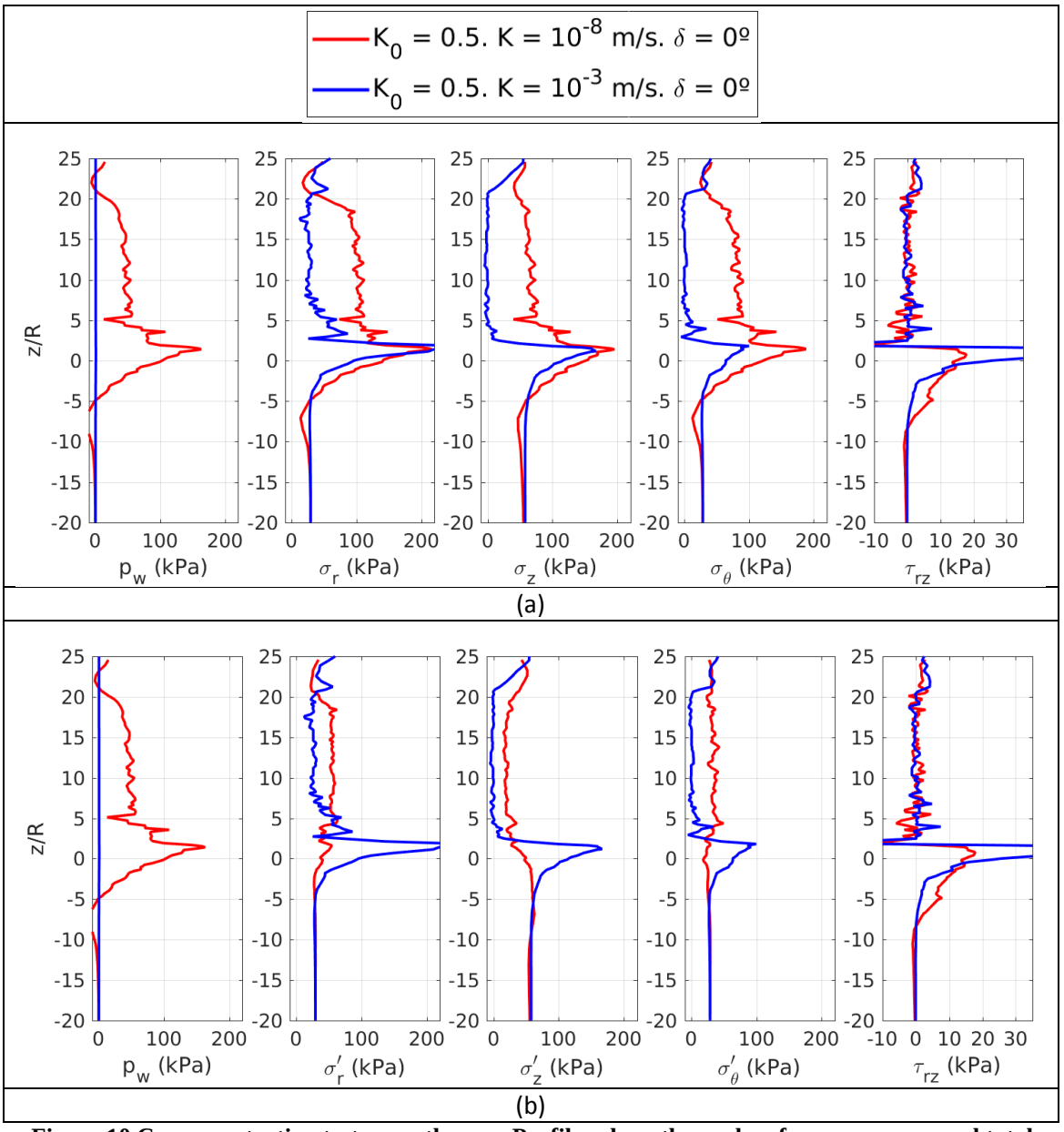

Figure 10 Cone penetration test, smooth cone. Profiles along the probe of pore pressure and total stress (a) or effective stress (b) for the two extreme values of permeability. The cone tip is located at Z/R = 0.

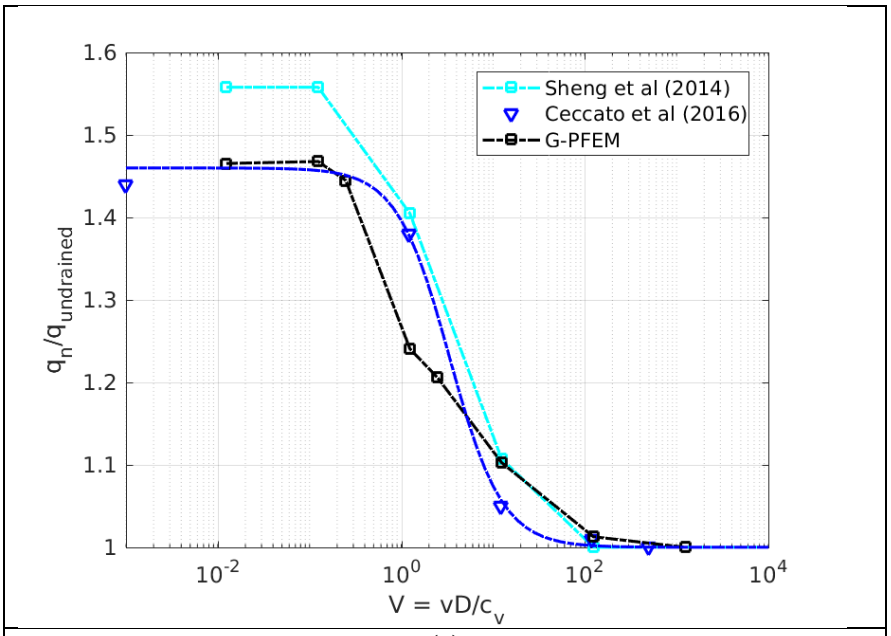

(a)

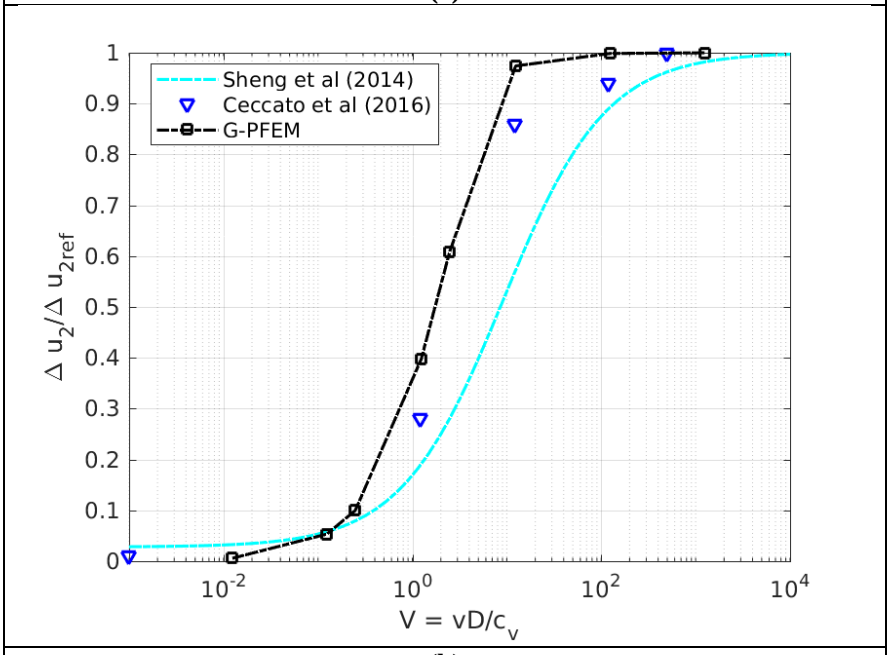

(b)

Figure 11 Simulated backbone curves for a frictionless CPTu in Cam Clay (a) cone tip resistance (b) excess pore pressure

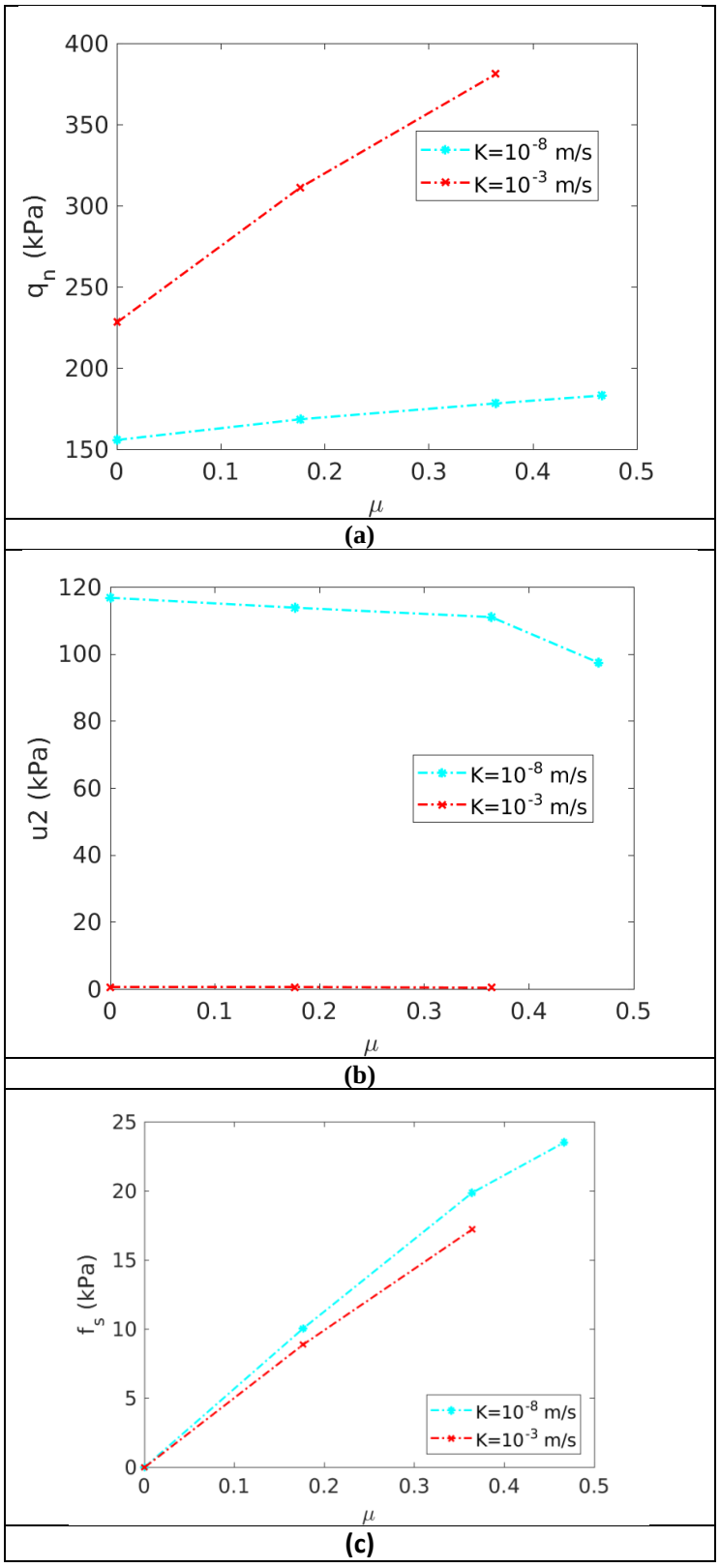

Figure 12 Cone penetration test. Influence of interface friction ratio for conditions of drained and undrained penetration on (a) net cone resistance (b) pore pressure at position 2 and (c) friction sleeve resistance.

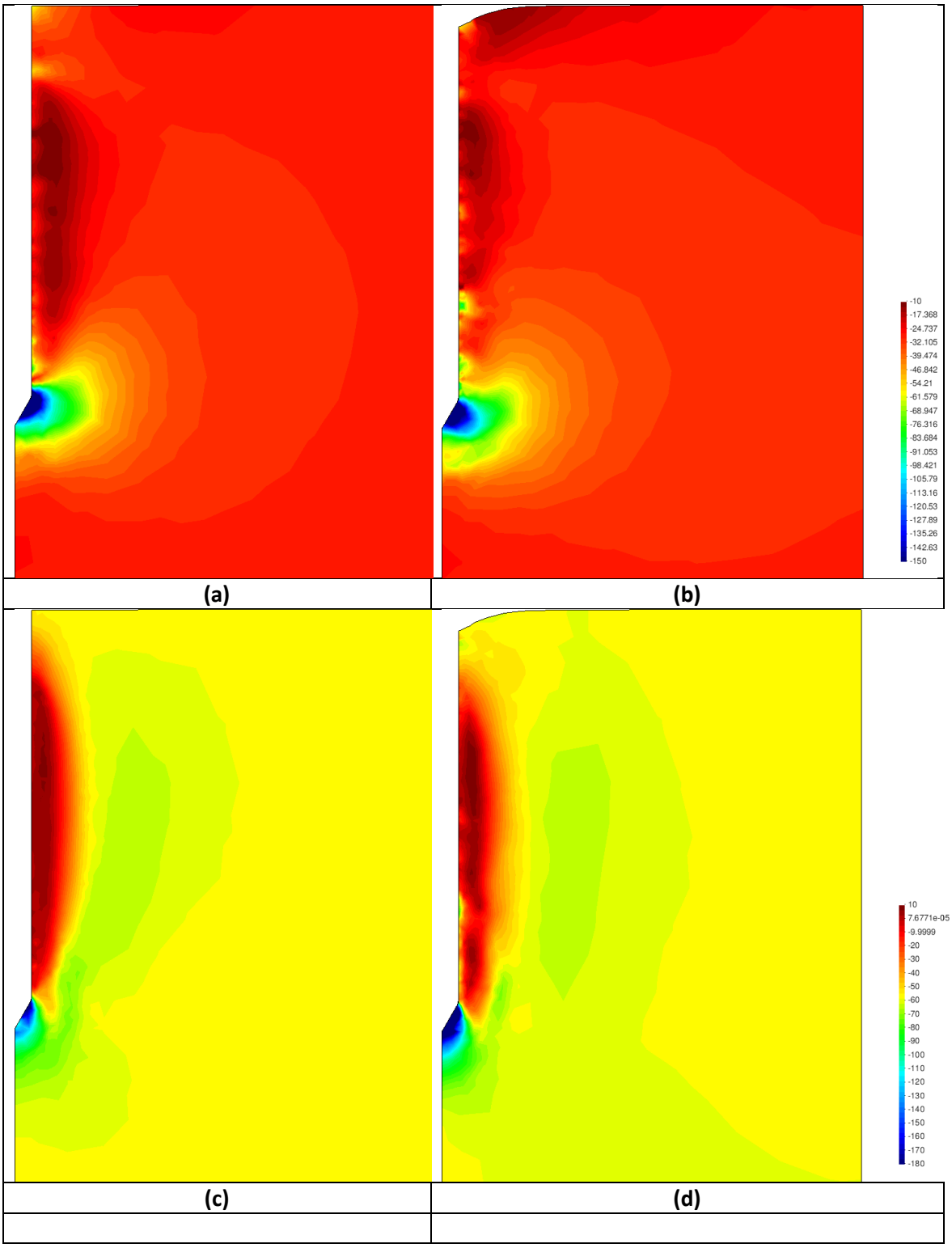

Figure 13 Effect of interface friction on stress fields around the CPTu (a) radial effective stress, drained, δ = 0; (b) radial effective stress, drained, δ = 20°; (c) vertical effective stress, drained, δ = 0; (d) vertical effective stress, drained, δ = 20°.

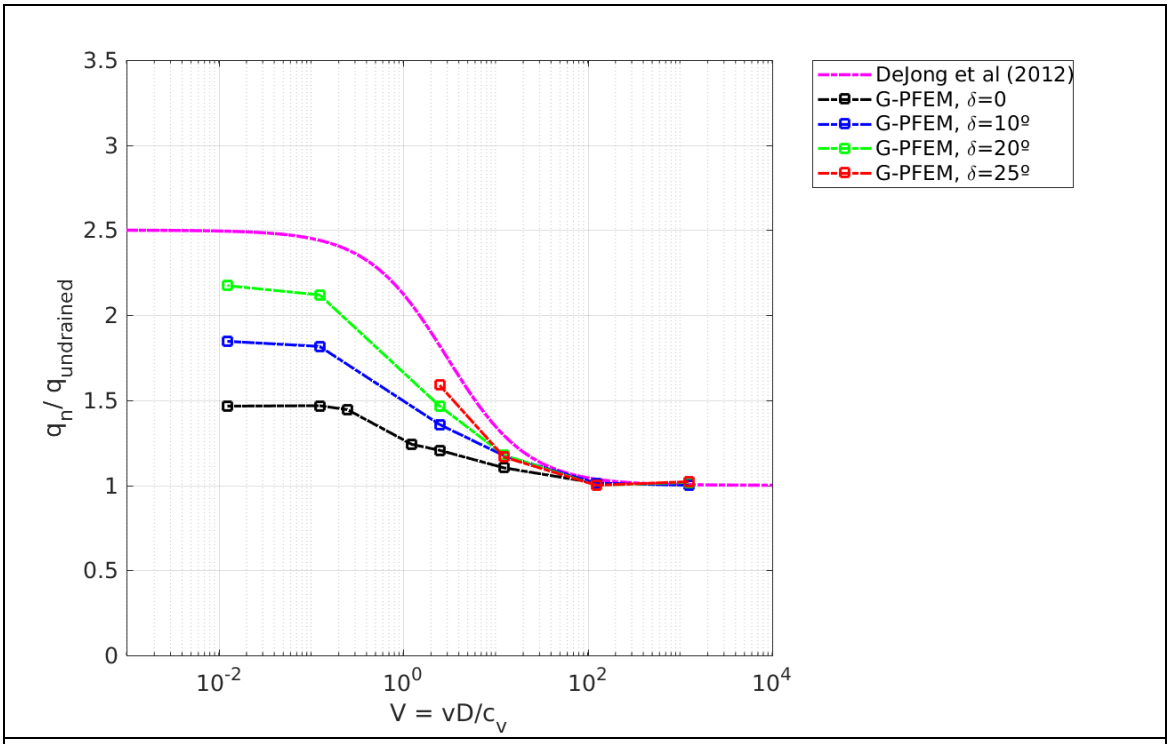

(a)

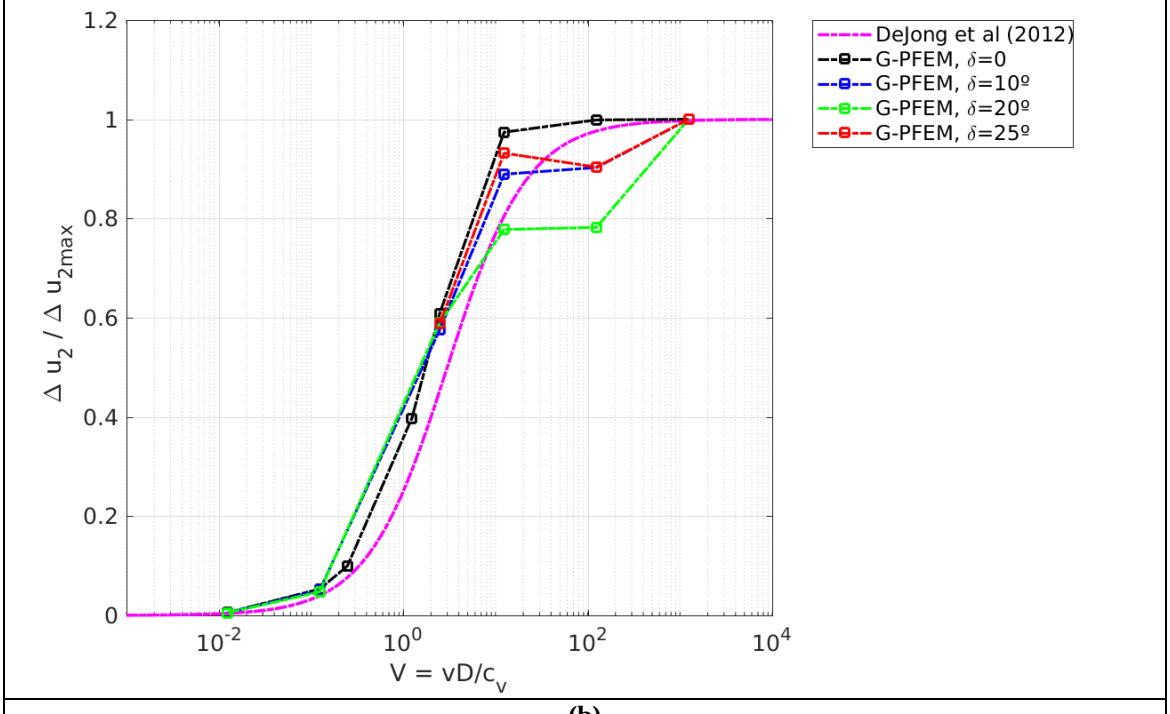

(b)

Figure 14 Effect of interface friction angle on simulated backbone curves for CPTu in Cam Clay (a) cone tip resistance (b) excess pore pressure

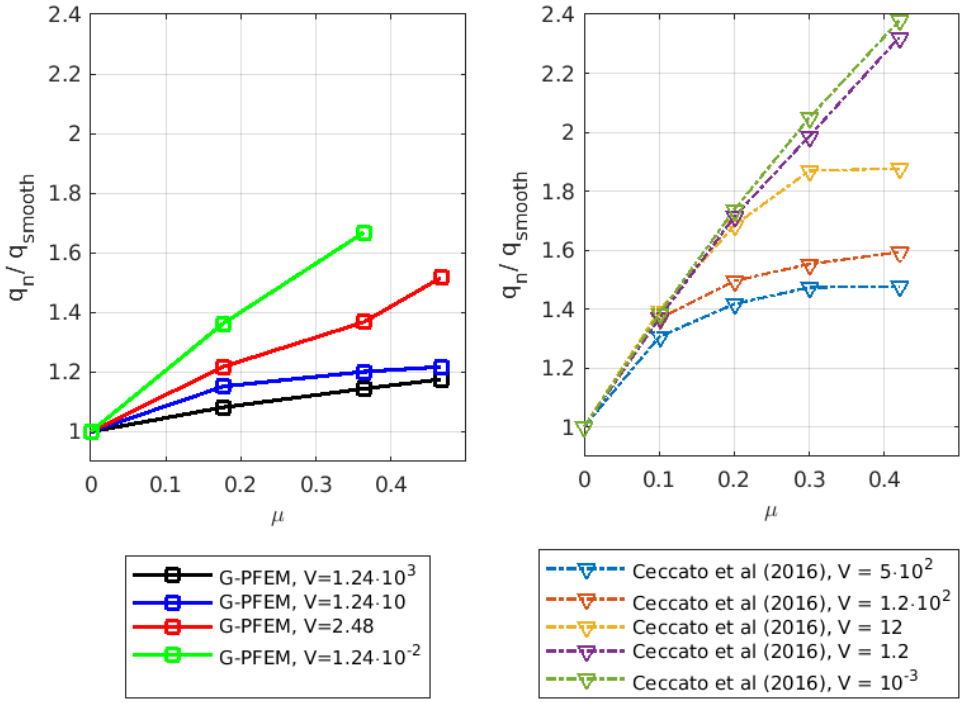

Figure 15 Effect of interface friction on net tip resistance increase for different normalized velocities